The fraction of ionizing radiation from massive stars that escapes to the intergalactic medium

N. R. Tanvir [1]★ J. P. U. Fynbo [2] A. de Ugarte Postigo,[3] J. Japelj,[4] K. Wiersema,[5,1]
D. Malesani,[2] D. A. Perley [6] A. J. Levan,[5] J. Selsing,[2] S. B. Cenko,[7,8] D. A. Kann,[3]
B. Milvang-Jensen,[2] E. Berger,[9] Z. Cano [3] R. Chornock,[10] S. Covino [11]
A. Cucchiara,[12] V. D'Elia,[13,14] A. Gargiulo,[15] P. Goldoni,[16] A. Gomboc,[17]
K. E. Heintz,[2,18] J. Hjorth,[2] L. Izzo [3] P. Jakobsson,[18] L. Kaper,[4] T. Krühler [19]
T. Laskar,[20] M. Myers,[21] S. Piranomonte,[13] G. Pugliese,[4] A. Rossi,[22]
R. Sánchez-Ramírez [3] S. Schulze,[23] M. Sparre [2,24] E. R. Stanway [5]
G. Tagliaferri,[11] C. C. Thöne,[3] S. Vergani,[25] P. M. Vreeswijk,[26] R. A. M. J. Wijers [4]
D. Watson[2] and D. Xu[27]

Affiliations are listed at the end of the paper

ABSTRACT

Whether stars could have driven the reionization of the intergalactic medium depends critically on the proportion of ionizing radiation that escapes the galaxies in which it is produced. Spectroscopy of gamma-ray burst (GRB) afterglows can be used to estimate the opacity to extreme ultraviolet (EUV) radiation along the lines-of-sight to the bursts. Assuming that long-duration GRBs trace the locations of the massive stars dominating EUV production, the average escape fraction of ionizing radiation can be calculated independently of galaxy size or luminosity. Here we present a compilation of H I column density (N_{HI}) measures for 140 GRBs in the range $1.6 < z < 6.7$. Although the sample is heterogeneous, in terms of spectral resolution and signal-to-noise ratio, fits to the Ly α absorption line provide robust constraints on N_{HI}, even for spectra of insufficient quality for other purposes. Thus we establish an escape fraction at the Lyman limit of $\langle f_{esc} \rangle \approx 0.005$, with a 98 per cent confidence upper limit of $\langle f_{esc} \rangle \approx 0.015$. This analysis suggests that stars provide a small contribution to the ionizing radiation budget at $z < 5$. At higher redshifts firm conclusions are limited by the small size of the GRB sample (7/140), but any decline in average H I column density seems to be modest. We also find no significant correlation of N_{HI} with galaxy UV luminosity or host stellar mass. We discuss in some detail potential biases and argue that, while not negligible, systematic errors in f_{esc} are unlikely to be more than a factor ~ 2 in either direction, and so would not affect the primary conclusions. Given that many GRB hosts are low-metallicity dwarf galaxies with high specific star-formation rates, these results present a particular problem for the hypothesis that such galaxies dominated the reionization of the Universe.

Key words: gamma-ray burst: general – intergalactic medium – galaxies: ISM – dark ages, reionization, first stars.

1 INTRODUCTION

A key question for our understanding of the reionization of hydrogen in the intergalactic medium (IGM) is the extent to which ionizing extreme ultraviolet (EUV) radiation from massive stars escapes from the galaxies in which it is produced. This can be parametrized

by the escape fraction, f_{esc}, the proportion of photons produced by stars at the Lyman limit wavelength ($\lambda = 912$ Å) that leave the virial radius of their host galaxy. Only if the average escape fraction, $\langle f_{esc} \rangle$, is sufficiently high in the era of reionization (EoR; $7 \lesssim z \lesssim 9$; Planck Collaboration XIII 2016), i.e. $\langle f_{esc} \rangle$ at least 0.1–0.2, is it likely that this phase change was predominantly driven by EUV star-light (e.g. Ouchi et al. 2009; Bouwens et al. 2012; Finkelstein et al. 2012; Robertson et al. 2015; Faisst 2016). Otherwise some other significant source of ionizing radiation is required, such as a large population of faint quasars (Madau & Haardt 2015; Khaire et al. 2016, but see Hassan et al. 2018 for counter arguments), X-ray binaries (Mirabel et al. 2011; Fragos et al. 2013; Knevitt et al. 2014; Madau & Fragos 2017) or decaying/annihilating particles (Sciama 1982; Hansen & Haiman 2004).

Direct searches for Lyman continuum emission below 912 Å in the rest frame are compromised by absorption due to neutral gas in the IGM (the Ly α forest), and essentially impossible above $z \sim 4$ as the IGM absorption becomes near total – the so-called Gunn–Peterson trough (Gunn & Peterson 1965). Observations at lower redshifts are still difficult, and there have been extensive efforts searching for such continuum emission from star-forming galaxies at $z = 2$–4 in recent years (e.g. Steidel, Pettini & Adelberger 2001; Shapley et al. 2006; Vanzella et al. 2010, 2012; Mostardi et al. 2013; Nestor et al. 2013; Vanzella et al. 2015; Japelj et al. 2017; Marchi et al. 2017). Results have been conflicting, particularly due to rare cases of low redshift galaxies aligning by chance with higher redshift targets (e.g. Vanzella et al. 2012; Siana et al. 2015), but given the scarcity of high escape fraction systems it appears that f_{esc} is not high on average (Grazian et al. 2017; Rutkowski et al. 2017). This is consistent with quasars being the primary source of EUV radiation maintaining a reionized IGM at $z < 4$. However, at least some individual cases at $z \gtrsim 3$ appear to have very high escape fractions $f_{esc} \gtrsim 0.5$ (de Barros et al. 2016; Shapley et al. 2016; Vanzella et al. 2016), and so might be analogues of galaxies in the EoR.

To account for the discrepancy between the expected and observed level of the escape fraction, it has been often suggested that $\langle f_{esc} \rangle$ may actually increase with decreasing galaxy luminosity and/or with increasing redshift (e.g. Razoumov & Sommer-Larsen 2010; Ciardi et al. 2012; Kuhlen & Faucher-Giguère 2012; Fontanot et al. 2014; Xu et al. 2016a; Anderson et al. 2017). Observationally, it is hard to reach sufficiently stringent constraints on the escape fraction for faint galaxy populations to investigate its dependence on luminosity (e.g. Japelj et al. 2017), while due to IGM absorption, the claim of a changing escape fraction with redshift can only be investigated through secondary means and simulations (e.g. Zackrisson, Inoue & Jensen 2013; Sharma et al. 2016). The challenge facing simulators is to model in sufficient detail the complex baryonic physics and radiative transfer given limited resolution, while also sampling a range of galaxies and environments. Typically, models of an instantaneous burst of star formation incorporating only single-star stellar evolution produce the large bulk of their EUV within a few Myr, limiting the time available for feedback from winds, radiation, and supernovae to open windows in the surrounding high-density gas. Recently, models that include binary stellar evolution have been shown to prolong the period of high EUV production to $\sim$10 Myr, and hence hold more promise for clearing of local gas, and for at least a relatively high fraction of stars leaving the immediate environment in which they formed (Ma et al. 2016; Stanway, Eldridge & Becker 2016).

An alternative approach, first performed by Chen, Prochaska & Gnedin (2007), to constraining $\langle f_{esc} \rangle$ empirically over a broad range

in redshift is via spectroscopy of long-duration gamma-ray burst (GRB) afterglows. These very bright, but short-lived, continuum sources allow detailed abundance studies of host galaxy gas along the line of sight. Crucially, this includes calculation of the neutral hydrogen column density, N_{HI}, in the host from fitting the Ly α absorption feature when it is seen (e.g. Prochaska et al. 2007; Fynbo et al. 2009). This column density can be directly converted into an opacity measure for EUV ionizing radiation and hence f_{esc}. For any individual host galaxy, a single sightline does not provide a robust measure of its average escape fraction, but since long-duration GRBs are associated with the core collapse of massive stars (e.g. Hjorth et al. 2003a; Xu et al. 2013), a sample of GRB afterglows should be representative of the distribution of all sightlines, specifically to the locations of young stars largely responsible for EUV production.

To date, neutral hydrogen columns reported for GRB hosts have generally been high, mostly classified as damped Ly α absorbers (DLAs; $\log(N_{HI}/\text{cm}^{-2}) > 20.3$), which is usually taken as being consistent with their massive-star progenitors remaining in or close to the dense molecular clouds in which they formed, and/or more generally residing at the hearts of gas-rich star-forming galaxies (e.g. Jakobsson et al. 2006). In fact, observations of the time-variability of fine-structure transitions in GRB afterglow spectra, in the (dozen or so) systems where it has been measured, has allowed the distance of the dominant absorbing clouds to be established, ranging from $\sim$50 pc to $\gtrsim$1 kpc (e.g. Vreeswijk et al. 2013). These scales are comparable to the sizes of large ionized superbubbles around star-forming regions in the low redshift Universe (Oey & Clarke 1997; Camps-Fariña et al. 2017), and so might indicate that absorption takes place due to neutral gas piled up at the boundaries of such bubbles for some GRBs. In any case, this tendency towards high column densities is potentially a problem since if the EUV escape fraction is to fulfil the requirements for reionization, a significant proportion of GRBs should have very low H I columns ($\log(N_{HI}/\text{cm}^{-2}) \ll 18$), particularly at $z > 5$.

This method has the considerable advantage that GRB afterglows readily probe gas in even very faint galaxies, for which either Lyman-continuum observations would be weakly constraining, or which may be missed completely in traditional galaxy surveys. In principle, then, with a sufficiently large sample one could trace the escape fraction both as a function of galaxy luminosity and of redshift. The tendency of GRBs to occur preferentially in lower metallicity galaxies, $Z/Z_{\odot} \lesssim 0.3$–1 (e.g. Japelj et al. 2016; Perley et al. 2016b; Graham & Fruchter 2017; Vergani et al. 2017), often dwarfs with high specific star formation rates (e.g. Svensson et al. 2010; Hunt et al. 2014), also suggests they should be more representative of the populations dominant during the EoR.

Chen et al. (2007), and subsequently Fynbo et al. (2009), conducted such an analysis, each obtaining 95 per cent confidence upper limits on $\langle f_{esc} \rangle$ of only $\sim$0.075 based on samples of $\sim$30 GRBs (with some overlap of their samples) in the redshift range $2 \lesssim z \lesssim 6$. Here we reinvestigate this issue, using a considerably larger sample of 140 GRBs with N_{HI} determinations, spanning a redshift range $1.6 \lesssim z \lesssim 6.7$. The structure of the paper is as follows: in Section 2 we present the sample of GRBs and describe its basic properties; in Section 3 we outline the implications for the average escape fraction of ionizing EUV radiation and consider evidence for evolution over cosmic history; in Section 4 we consider a range of potential systematic uncertainties that could bias our conclusions in either direction, and address more fully the question of how representative GRB sightlines are likely to be for the stellar populations of inter-

est for reionization; finally in Section 5 we draw our conclusions. Further details of some individual GRBs, including results not already reported elsewhere, are given in the Appendix.

2 THE H I COLUMN-DENSITY SAMPLE

Spectra of GRB afterglows frequently exhibit strong Lyα absorption lines that can be modelled to constrain the column density of neutral hydrogen responsible. Particularly at higher redshifts, this relies largely on fitting the red wing of the line, since absorption by the IGM Lyα forest significantly affects the blue wing. In the large majority of cases, the systemic redshifts are known quite precisely from metal-line detections, which improves the precision of the Lyα fits. We have gathered together H I column densities towards GRBs from the literature, and combined them with a large number of new measurements we have made using afterglow spectra from various sources. Many of these come from the long-running Very Large Telescope (VLT) X-shooter legacy programme (Selsing et al. 2018), but we also include data from the Nordic Optical Telescope (NOT), the William Herschel Telescope (WHT), the Gran Telescopio Canarias (GTC), the Telescopio Nazionale Galileo (TNG), the Gemini Telescopes (both North and South), the Asiago Copernico Telescope (CT), the Keck Telescope, the Large Binocular Telescope (LBT), as well as other VLT spectrographs. The bulk of the GRBs were originally discoveries of the Neil Gehrels *Swift* Observatory, but there was little consistency in terms of which bursts were followed-up or the kinds of observations obtained (e.g. in terms of spectral resolution, wavelength coverage, sensitivity etc.). The net result is an inhomogeneous sample, and potential effects of selection biases are discussed in Section 4.

The H I column densities measured from the afterglow spectra in our sample are plotted in Fig. 1 and summarized in Table 1; corresponding primary sources for the adopted values of $\log(N_{HI})$ are given in the fourth column of the table, and readers are referred also to Appendix A for further details regarding previously unreported fits and additional comments on some particular cases. The total number of sightlines is 140, which represents a more than fourfold increase over similar previous studies (Chen et al. 2007; Fynbo et al. 2009).

The median redshift of our sample is $\bar{z} = 2.80$. The lower redshift cut-off, at $z \sim 1.6$, occurs because the observed wavelength of Lyα falls in the near-UV, and begins to be strongly affected by declining atmospheric transmission. At the high redshift end, the sample is curtailed due to declining spectral quality; although bursts at $z \gtrsim 6.7$ have been found, either the signal-to-noise has been too poor to reliably measure the red damping wing of Lyα (Salvaterra et al. 2009; Tanvir et al. 2009; Tanvir et al. 2018) or the redshift has been inferred photometrically (Cucchiara et al. 2011a; Bolmer et al. 2018b).

3 IMPLICATIONS FOR THE IONIZING ESCAPE FRACTION

Following Chen et al. (2007), we note that the optical depth for radiation at the Lyman limit (912 Å) along a given sightline due to absorption by neutral hydrogen is given by $\tau = \sigma_{LL} N_{HI}$, where $\sigma_{LL} = 6.28 \times 10^{-18}$ cm^2 is the photoionization cross-section of hydrogen. Hence, the average escape fraction for n sightlines is given by

$$\langle f_{esc} \rangle = \frac{1}{n} \sum_{i=1}^{n} \exp(-\tau_i). \tag{1}$$

Considering our whole sample, we find a mean value of only $\langle f_{esc} \rangle = 0.005$, well below that thought to be required in the EoR.

In Fig. 2 we plot the cumulative distribution of H I column density measures for the whole sample. The median value of column density is $\log(N_{HI}/\text{cm}^{-2}) = 21.59$, consistent with previous studies (e.g. the equivalent figure is 21.5 for the sample of Fynbo et al. 2009) and also similar to the median values of $\log(N_{HI})$ towards H II regions in the Magellanic Clouds (see Fig. 1; Pellegrini et al. 2012). We find that up to the median point the sample is well described by a simple power-law distribution $P(<x) \propto x^{0.4}$, where x is the value of N_{HI}, shown as an orange dashed line in the figure. While this model is not motivated by any particular physical considerations, it does provide a smooth representation of the data, and using it we obtain an average escape fraction $\langle f_{esc} \rangle = 0.004$, in good agreement with the value found above.

Most of the rest of this paper is concerned with the robustness of this result, and the statistical and potential systematic uncertainties that may affect it.

3.1 Low column density sightlines

Only two sightlines have $\log(N_{HI}/\text{cm}^{-2}) < 18$ (corresponding to $f_{esc} > 0.002$), and as it happens both of these low column density systems were already included in the Chen et al. (2007) and Fynbo et al. (2009) analyses. Since the numerical result for $\langle f_{esc} \rangle$ depends entirely on these two sightlines, we review here what is known of their properties and in particular consider whether there could be attenuation of EUV radiation by dust as well as H I absorption. We also address the effect of direct recombinations to the ground-state producing ionizing photons.

3.1.1 GRB 050908

GRB 050908, at $z = 3.34$, had a moderately bright optical afterglow, being $R \approx 19$ at 15 min post-burst (Torii 2005). Spectroscopy was obtained with Gemini/GMOS, from which Chen et al. (2007) reported a column density of $\log(N_{HI}/\text{cm}^{-2}) = 19.1$. The lower value of $\log(N_{HI}/\text{cm}^{-2}) = 17.6$, corresponding to $f_{esc} = 0.08$, used here, was that derived from a VLT/FORS1 spectrum (Fynbo et al. 2009), and it is preferred since it is based on direct evidence of non-zero afterglow continuum emission below the Lyman limit.

There is no indication of excess absorption in the *Swift* X-ray observations[1] (Evans et al. 2009), which is also consistent with a low column density and low extinction sightline.

3.1.2 GRB 060607A

GRB 060607A, at $z = 3.08$, had a very bright and well-studied early optical afterglow, which reached $r = 14.3$ at 3 min post-burst (Nysewander et al. 2009). This sightline has the lowest column density of our sample at $\log(N_{HI}/\text{cm}^{-2}) = 16.95$, from a VLT/UVES spectrum (Fynbo et al. 2009), corresponding $f_{esc} = 0.57$. The spectrum also showed evidence for emission below the Lyman limit, although only for a small stretch of wavelength before it was cut-off by an intervening absorber, but this is consistent with a very low opacity.

The light curve and spectral energy distribution were studied in detail by Nysewander et al. (2009), who modelled their *Bgri* optical data together with *H*-band photometry from Molinari et al. (2007). They concluded that a rest-frame dust extinction of zero was

---

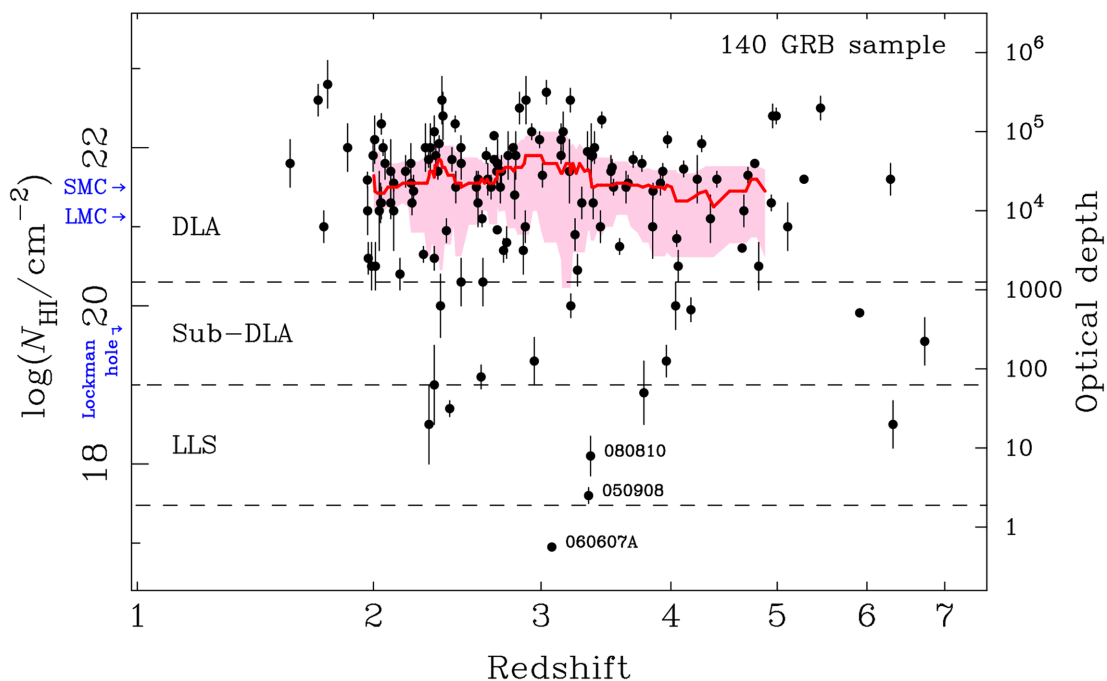[1] http://www.swift.ac.uk/xrt_spectra/00154112/

Figure 1. The values of neutral hydrogen column density in the host plotted against redshift for the sample of GRBs. The corresponding optical depth at the Lyman limit is shown on the right-hand axis. The large majority are DLAs, with a smaller proportion (17/140) being classified as sub-DLAs, Lyman Limit Systems (LLS) and below. All sightlines apart from the two with the lowest column densities are essentially opaque ($\tau \gtrsim 10$) to EUV ionizing radiation. The running median (red line) and interquartile range (pink shading) of 20 points shows no evidence for significant variation with redshift. For comparison, on the left axis we also mark the locations of the median $\log(N_{\mathrm{H\,I}}/2)$ values in the directions of LMC and SMC H II regions from Pellegrini et al. (2012) (halving the measured columns is appropriate since they include contributions from both the foreground and background of the H II region), and the lowest column density out of the Milky Way from the position of the Sun, the 'Lockman hole' (Lockman, Jahoda & McCammon 1986).

ruled out at the 2.6σ level. The shape of the extinction law is only weakly constrained by these data, so extrapolating to the Lyman limit introduces a large systematic uncertainty, but with reasonable dust laws their favoured extinction would correspond to a value of $A_{912} \gtrsim 1$. If this inference is correct, then it would suggest the actual escape fraction at the Lyman limit for GRB 060607A could be significantly diminished by dust extinction, by a factor $\sim$2.5 or more.

We note that there is also marginal evidence of X-ray absorption[2] in the source-frame at a level of $N_{\mathrm{H,\,X}} \approx (3.1 \pm 1.9) \times 10^{21}\,\mathrm{cm}^{-2}$ (Evans et al. 2009) over the Milky Way foreground (Willingale et al. 2013). This would be broadly consistent with an SMC dust-to-gas ratio (Bouchet et al. 1985) provided the hydrogen associated with this gas had largely been ionized (so it was not seen in the optical spectrum) but the dust had mostly not been destroyed. On the other hand, Prochaska et al. (2008) argue that the absence of N V absorption argues for both low density and low metallicity surrounding the burst location.

3.1.3 Direct recombinations to the ground-state

Gas that has been ionized by massive star radiation within a host galaxy will generally recombine quickly. A fraction of recombining H ions will go directly to the ground-state, and so emit a photon just above the Lyman limit energy (some higher energy photons will also be emitted by recombining He ions). In low column density

systems a fraction of these will escape the host without further absorption, and therefore re-boost the escaping ionizing flux, albeit with radiation that will soon be redshifted to energies below 1 Ryd. In other words, simply translating H I column density into line-of-sight opacity is likely to lead to a small underestimate of the escape fraction in low column density systems. The net effect of this re-boost depends on various factors, but could provide an increase of up to 10–20 per cent in the effective escape fraction (Faucher-Giguère et al. 2009), thus at least partially offsetting any dust extinction.

For the remainder of Section 3 we will continue to consider only the opacity due to H I absorption, but will return to the potential systematic effects of dust in Section 4.1.1.

3.2 Statistical uncertainty

Even with our considerably larger sample of sightlines, the fact that only two have any appreciable escape fraction means that to some extent we are still dealing with rather small number statistics. We also lack a robust theoretical model that could be fit to the data, and so must explore the statistical uncertainties non-parametrically.

Again we first follow Chen et al. (2007) by performing a bootstrap exercise, employing 10^6 random resamples of the data with replacement. From this we estimate a 98 per cent confidence upper limit of $\langle f_{\mathrm{esc}} \rangle < 0.015$; the result is the same whether or not we allow the resampled $N_{\mathrm{H\,I}}$ values to have additional scatter based on the error bars for each point.

In an alternative approach, we simulated several large populations of sightlines with higher values of average escape fraction than found in our data (by replicating the GRB 050908/060607A values),

[2]http://www.swift.ac.uk/xrt_spectra/00213823/

Table 1. The sample of GRBs. References: (1) Jensen et al. (2001), (2) Fynbo et al. (2002), (3) Vreeswijk et al. (2006), (4) Hjorth et al. (2003b), (5) Fynbo et al. (2005), (6) Møller et al. (2002), (7) Shin et al. (2006), (8) Vreeswijk et al. (2004), (9) Jakobsson et al. (2004), (10) Fynbo et al. (2009), (11) Berger et al. (2006), (12) Totani et al. (2006), (13) Chen et al. (2007), (14) Chary, Berger & Cowie (2007), (15) Ferrero et al. (2009), (16) This work, (17) Wiseman et al. (2017), (18) Patel et al. (2010), (19) de Ugarte Postigo et al. (2012), (20) Kuin et al. (2009), (21) D'Avanzo et al. (2010), (22) Savaglio et al. (2012), (23) Levesque et al. (2010a), (24) Selsing et al. (2018), (25) Cucchiara et al. (2011b), (26) Zafar et al. (2018b), (27) Cucchiara et al. (2015), (28) Jeong et al. (2014), (29) Chornock et al. (2014), (30) Melandri et al. (2015), (31) Pugliese et al. in preparation, (32) Chen et al. (2009), (33) Perley (2011), (34) Schulze et al. (2015), (35) Greiner et al. (2015b), (36) McGuire et al. (2016), (37) Tanvir et al. (2012a), (38) McGuire et al. in preparation, (39) Thöne et al. (2011), (40) Friis et al. (2015), (41) Perley et al. (2013), (42) Laskar, Berger & Chary (2011), (43) Perley et al. (2016b), (44) Myers et al. in preparation (in this case, the derived *Spitzer* photometry was transformed to stellar mass estimates following Perley et al. 2016b).

GRB	z	$\log\left(\frac{N_{HI}}{cm^{-2}}\right)$	Refs	$M_{UV,\,AB}$	Refs	$\log(M_*/M_\odot)$	Refs
000301C	2.03	21.20 ± 0.50	(1)	-16.0 ± 0.5	(32)	–	–
000926*	2.04	21.30 ± 0.25	(2)	-20.40 ± 0.07	(32)	9.64	(41)
011211*	2.14	20.40 ± 0.20	(3)	-19.97 ± 0.10	(32)	8.0	(41)
020124*	3.20	21.70 ± 0.40	(4)	>-15.72	(35)	<9.90	(42)
021004*	2.33	19.00 ± 0.50	(5),(6),A1	-20.56 ± 0.10	(5)	9.45	(41)
030226	1.99	20.50 ± 0.30	(7)	–	–	–	–
030323*	3.37	21.90 ± 0.07	(8)	-18.47 ± 0.1	(32)	<9.85	(42)
030429*	2.65	21.60 ± 0.20	(9)	–	–	–	–
050319*	3.24	20.90 ± 0.20	(10)	>-20.01	(33)	9.69	(43)
050401*	2.90	22.60 ± 0.30	(10)	-19.28 ± 0.31	(34)	9.61	(43)
050505*	4.27	22.05 ± 0.10	(11)	–	–	<9.67	(44)
050730*	3.97	22.10 ± 0.10	(10)	>-17.21	(35)	<9.46	(43)
050820A*	2.61	21.10 ± 0.10	(10)	-18.93 ± 0.06	(34)	9.38	(43)
050904*	6.29	21.60 ± 0.20	(12)	-19.21 ± 0.2	(36)	<10.07	(43)
050908*	3.34	17.60 ± 0.10	(10)	-18.18 ± 0.27	(34)	<9.91	(42)
050922C*	2.20	21.55 ± 0.10	(10)	>-17.95	(33)	<9.01	(43)
060115*	3.53	21.50 ± 0.10	(10)	-18.61 ± 0.27	(34)	9.43	(43)
060124*	2.30	18.50 ± 0.50	(10)	–	–	–	–
060206*	4.05	20.85 ± 0.10	(10)	-18.47 ± 0.1	(35)	<9.95	–
060210*	3.91	21.55 ± 0.15	(10)	-21.85 ± 0.12	(33)	10.46	(43)
060223A*	4.41	21.60 ± 0.10	(13)	-18.33 ± 0.15	(35)	<10.17	(42)
060510B*	4.94	21.30 ± 0.10	(13)	-20.51 ± 0.17	(35)	9.86	(44)
060522	5.11	20.60 ± 0.30	(14),(16)	>-18.34	(37)	<9.31	(43)
060526*	3.21	20.00 ± 0.15	(10)	>-17.36	(35)	9.30	(43)
060605	3.77	18.90 ± 0.40	(15)	-17.94 ± 0.2	(35)	<9.97	(42)
060607A*	3.08	16.95 ± 0.03	(10)	>-15.52	(35)	<9.45	(43)
060707*	3.43	21.00 ± 0.20	(10)	-20.78 ± 0.06	(34)	9.99	(43)
060714*	2.71	21.80 ± 0.10	(10)	-18.88 ± 0.28	(34)	9.25	(43)
060906*	3.69	21.85 ± 0.10	(10)	>-20.60	(35)	<10.02	(42)
060926*	3.21	22.60 ± 0.15	(10)	-21.59 ± 0.05	(35)	10.71	(42)
060927*	5.47	22.50 ± 0.15	(10)	>-18.01	(37)	<9.63	(43)
061110B*	3.44	22.35 ± 0.10	(10)	-19.82 ± 0.29	(35)	<9.47	(43)
070110*	2.35	21.70 ± 0.10	(10)	-19.81 ± 0.11	(34)	<9.16	(43)
070411*	2.95	19.30 ± 0.30	(10)	–	–	–	–
070506	2.31	22.00 ± 0.30	(10)	-18.80 ± 0.21	(34)	–	–
070611*	2.04	21.30 ± 0.20	(10)	>-17.52	(34)	–	–
070721B	3.63	21.50 ± 0.20	(10)	-18.39 ± 0.44	(35)	<9.42	(43)
070802	2.45	21.50 ± 0.20	(10)	-19.85 ± 0.2	(34)	9.69	(41)
070810A*	2.17	21.70 ± 0.20	(16)	–	–	–	–
071031*	2.69	22.15 ± 0.05	(10)	–	–	–	–
080129	4.35	21.10 ± 0.30	(16)	–	–	<11.47	(44)
080210*	2.64	21.90 ± 0.10	(10)	>-19.32	(33)	<9.50	(43)
080310*	2.43	18.70 ± 0.10	(10)	>-18.45	(33)	9.78	(43)
080413A*	2.43	21.85 ± 0.15	(10)	–	–	<9.64	(43)
080603B*	2.69	21.85 ± 0.05	(10)	–	–	9.15	(43)
080607*	3.04	22.70 ± 0.15	(10)	-19.4 ± 0.5	(35)	10.45	(43)
080721*	2.59	21.60 ± 0.10	(10)	–	–	<9.63	(43)
080804*	2.20	21.30 ± 0.15	(10)	–	–	9.28	(43)
080810*	3.36	18.10 ± 0.25	(17),A6	-22.43 ± 0.5	(35)	10.29	(44)
080905B	2.37	22.60 ± 0.30	(16)	–	–	–	–
080913	6.73	19.55 ± 0.30	(18),A8	>-17.28	(38)	–	–
081008*	1.97	21.59 ± 0.10	(19)	–	–	9.18	(43)
081029*	3.85	21.45 ± 0.10	(16)	>-19.87	(35)	<9.39	(43)
081118	2.58	21.50 ± 0.20	(16)	–	–	9.18	(43)

Table 1 – *continued*

GRB	z	$\log\left(\frac{N_{HI}}{cm^{-2}}\right)$	Refs	$M_{UV, AB}$	Refs	$\log(M_*/M_\odot)$	Refs
081203A*	2.05	22.00 ± 0.10	(20)	–	–	–	–
081222*	2.77	20.80 ± 0.20	(16)	–	–	9.61	(43)
090205*	4.65	20.73 ± 0.05	(21)	-21.26 ± 0.13	(35)	<10.7	(21)
090313	3.38	21.30 ± 0.20	(16)	>-21.19	(35)	<10.35	(44)
090323*	3.58	20.75 ± 0.10	(22),A13	-21.60 ± 0.18	(35)	10.58	(44)
090426*	2.61	19.10 ± 0.15	(23),A14	-20.43 ± 0.08	(39)	–	–
090516A*	4.11	21.73 ± 0.10	(19)	-20.99 ± 0.4	(35)	10.63	(44)
090519	3.85	21.00 ± 0.40	(16)	>19.09	(35)	<10.35	(43)
090529	2.62	20.30 ± 0.30	(16)	–	–	–	–
090715B*	3.01	21.65 ± 0.15	(16)	–	–	10.20	(44)
090726	2.71	21.80 ± 0.30	(16)	–	–	–	–
090809*	2.74	21.70 ± 0.20	(24)	–	–	–	–
090812*	2.45	22.30 ± 0.10	(19)	–	–	<9.35	(43)
090926A*	2.11	21.55 ± 0.10	(24)	–	–	–	–
091029*	2.75	20.70 ± 0.15	(16)	–	–	<9.81	(43)
100219A*	4.67	21.20 ± 0.20	(24)	-19.74 ± 0.5	(35)	<10.11	(44)
100302A	4.81	20.50 ± 0.30	(16)	–	–	–	–
100316A	3.16	22.20 ± 0.25	(16)	–	–	–	–
100425A	1.76	21.00 ± 0.20	(24)	–	–	–	–
100513A*	4.77	21.80 ± 0.05	(16)	-19.88 ± 0.29	(35)	<10.14	(44)
100728B	2.11	21.20 ± 0.50	(24)	–	–	<9.25	(43)
110128A*	2.34	21.90 ± 0.15	(24)	–	–	–	–
110205A*	2.21	21.45 ± 0.20	(25)	–	–	9.72	(43)
110731A*	2.83	21.90 ± 0.30	(16)	–	–	–	–
110818A	3.36	21.90 ± 0.40	(24)	-21.68 ± 0.05	(35)	–	–
111008A*	4.99	22.40 ± 0.10	(24)	>-20.80	(35)	–	–
111107A*	2.89	21.00 ± 0.20	(24)	–	–	–	–
120119A	1.73	22.60 ± 0.20	(24)	–	–	9.91	(43)
120327A*	2.81	22.00 ± 0.05	(24)	–	–	–	–
120404A	2.88	20.70 ± 0.30	(24)	–	–	–	–
120712A	4.17	19.95 ± 0.15	(24)	–	–	<9.82	(44)
120716A*	2.49	22.00 ± 0.15	(24)	–	–	–	–
120811C*	2.67	21.50 ± 0.15	(16)	–	–	–	–
120815A*	2.36	22.05 ± 0.10	(24)	–	–	–	–
120909A*	3.93	21.70 ± 0.10	(24)	-21.16 ± 0.12	(35)	–	–
121024A*	2.30	21.85 ± 0.10	(24)	-21.47 ± 0.10	(40)	9.9	(40)
121027A	1.77	22.80 ± 0.30	(24),A25	–	–	–	–
121128A	2.20	21.80 ± 0.25	(16)	–	–	–	–
121201A	3.39	22.00 ± 0.20	(24)	-20.84 ± 0.21	(35)	–	–
121229A	2.71	21.70 ± 0.20	(24)	–	–	–	–
130408A*	3.76	21.80 ± 0.10	(24)	>-21.13	(35)	–	–
130427B	2.78	21.90 ± 0.30	(24)	–	–	–	–
130505A*	2.27	20.65 ± 0.10	(27)	–	–	–	–
130518A*	2.49	21.80 ± 0.20	(16)	–	–	–	–
130606A*	5.91	19.91 ± 0.02	(24)	-20.33 ± 0.15	(36)	–	–
130610A*	2.09	21.30 ± 0.20	(16)	–	–	–	–
130612A*	2.01	22.10 ± 0.30	(24)	–	–	–	–
131011A*	1.87	22.00 ± 0.30	(24)	–	–	–	–
131108A*	2.40	20.95 ± 0.15	(16)	–	–	–	–
131117A	4.04	20.00 ± 0.30	(24)	–	–	–	–
140206A	2.73	21.50 ± 0.20	(16)	–	–	–	–
140226A	1.97	20.60 ± 0.20	(27)	–	–	–	–
140304A*	5.28	21.60	(28)	–	–	–	–
140311A*	4.95	22.40 ± 0.15	(24)	–	–	<10.10	(44)
140419A*	3.96	19.30 ± 0.20	(27)	–	–	–	–
140423A*	3.26	20.45 ± 0.20	(27)	–	–	–	–
140430A	1.60	21.80 ± 0.30	(24)	–	–	–	–
140515A	6.32	18.50 ± 0.30	(29),(30),A31	-18.31 ± 0.35	(36)	–	–
140518A*	4.71	21.65 ± 0.10	(27)	–	–	–	–
140614A	4.23	21.60 ± 0.30	(24)	–	–	–	–
140629A	2.28	22.00 ± 0.30	(16)	–	–	–	–
140703A*	3.14	21.90 ± 0.10	(16)	–	–	–	–
140808A*	3.29	21.30 ± 0.20	(16)	–	–	–	–
141028A*	2.33	20.60 ± 0.15	(24)	–	–	–	–

Table 1 – *continued*

GRB	z	$\log\left(\frac{N_{HI}}{cm^{-2}}\right)$	Refs	$M_{UV, AB}$	Refs	$\log(M_*/M_\odot)$	Refs
141109A*	2.99	22.10 ± 0.10	(24)	–	–	–	–
150206A	2.09	21.70 ± 0.40	(24)	–	–	–	–
150403A*	2.06	21.80 ± 0.20	(24)	–	–	–	–
150413A*	3.14	22.10 ± 0.20	(16)	–	–	–	–
150915A	1.97	21.20 ± 0.30	(24)	–	–	–	–
151021A*	2.33	22.20 ± 0.20	(24)	–	–	–	–
151027B*	4.06	20.50 ± 0.20	(24)	–	–	–	–
151215A	2.59	21.30 ± 0.30	(16)	–	–	–	–
160203A*	3.52	21.75 ± 0.10	(24),(31)	–	–	–	–
160227A	2.38	22.40 ± 0.30	(16)	–	–	–	–
160629A*	3.33	21.95 ± 0.25	(16)	–	–	–	–
161014A	2.82	21.40 ± 0.30	(24)	–	–	–	–
161017A	2.01	20.50 ± 0.30	(16)	> -20.11	(16)	–	–
161023A*	2.71	20.96 ± 0.05	(24)	–	–	–	–
170202A*	3.65	21.55 ± 0.10	(24)	–	–	–	–
170405A*	3.51	21.70 ± 0.20	(16)	–	–	–	–
170531B	2.37	20.00 ± 0.40	(16)	–	–	–	–
180115A	2.49	20.30 ± 0.30	(16)	–	–	–	–
180325A*	2.04	22.30 ± 0.14	(26)	–	–	–	–
180329B	2.00	21.90 ± 0.20	(16)	–	–	–	–
180624A*	2.86	22.50 ± 0.20	(16)	–	–	–	–
181020A*	2.94	22.20 ± 0.10	(16)	–	–	–	–

Note: * denotes bursts included in the high-quality sub-sample (Section 3.6).
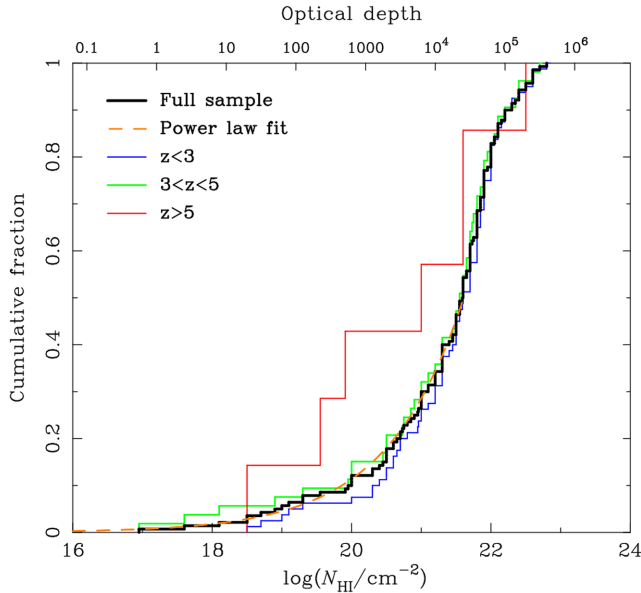
Figure 2. Cumulative distribution of H I for the whole sample and split into subsets by redshift, as indicated. The corresponding optical depth at Ly α is shown on the top axis. A power-law fit to the lower column density half of the sample is shown by the orange dashed line (see the text).

and drew 10^5 random 140-member samples from each of these. For the case of the population with $\langle f_{esc}\rangle_{pop} = 0.02$ we found 98 per cent of random samples produced $\langle f_{esc}\rangle_{samp} > 0.005$. Thus, these two methods agree on an upper limit for $\langle f_{esc}\rangle$ of 0.015–0.02. A similar analysis gives a 98 per cent lower limit of $\langle f_{esc}\rangle > 10^{-3}$.

These are significantly tighter constraints than found by the previous studies of Chen et al. (2007) and Fynbo et al. (2009) of $\langle f_{esc}\rangle < 0.075$ at 95 per cent, due to our larger sample size and the fact

that no further very low column-density sightlines have been identified in any of the additional GRBs. We note that our result is also consistent with the $\langle f_{esc}\rangle = 0.020 \pm 0.017$ obtained by constraining the flux below the Lyman-limit in a stacked spectrum of 11 GRB afterglows with $\bar{z} = 3.66$ by Christensen et al. (2011).

3.3 Comparison to model predictions

It is worth noting that our N_{HI} distribution is inconsistent with the predictions of Cen & Kimm (2014) who used high-resolution cosmological radiation-hydrodynamic simulations of galaxies within the EoR ($z \sim 7$) to explore column densities along GRB sightlines. They found a bimodal distribution with a peak at high column density ($\log(N_{HI}/cm^{-2}) \sim 21$–22), similar to the observed distribution, but then another substantial peak with column densities $\log(N_{HI}/cm^{-2}) < 18$ which is not seen in practice. Part of the explanation could be that Cen & Kimm (2014) assumed that the GRB rate traces the SNII rate and found a large fraction of their low column-density GRBs occurred in supersolar metallicity environments, whereas in reality GRB progenitors seem to be younger at explosion (e.g. Larsson et al. 2007) and crucially, unlike SNII, are rarely found in high-metallicity galaxies (e.g. Perley et al. 2015). On the other hand, their simulations do not account for the effect of GRBs in ionizing gas local to the burst (see Section 4.1.2), and it seems when a high column density is found in their models it is often due to such local gas, whereas the low column-density cases occur for progenitors that have escaped their birth clouds. This suggests that their simulations do not capture the distributed nature of neutral hydrogen in these star-forming galaxies, at least as it is found in $z \sim 2$–5 GRB hosts.

Our results do correspond much more closely with the earlier simulations of Pontzen et al. (2010), who similarly investigated sightlines to young star forming regions in model galaxies, but in this case did specifically consider the $z \sim 2$–5 range. They found

a median $\log(N_{\rm HI}/{\rm cm}^{-2})$ of 21.5 and calculated an escape fraction of $\langle f_{\rm esc} \rangle \approx 0.01$, both close to our findings. Indeed, their default prescription assumes that GRBs trace star formation up to an age of 50 Myr, whereas restricting to a perhaps more realistic 10 Myr age reduces $\langle f_{\rm esc} \rangle$ to 0.007. These simulations included the effect of local ionizing sources on the gas proximate to the burst, but again not the potential additional effect of ionization due to the GRB itself. We return to these issues in Section 4.

3.4 Evolution with redshift

As shown by the red line in Fig. 1, there is no evidence for significant variation in the median value of $\log(N_{\rm HI})$ between redshifts $z \sim 2$ to $z \sim 5$. To investigate this further, in Fig. 2 we plot cumulative $N_{\rm HI}$ distributions for three subsets of the whole sample cut in redshift. It is apparent that there is little difference between the low ($z < 3$) and intermediate redshift ($3 < z < 5$) sub-samples – the median values are the very similar, and a two-sample Kolmogorov–Smirnov (KS) test finds them to be consistent with the null hypothesis that they are drawn from the same parent distribution (p value of 0.75). The intermediate redshift sub-sample does have a somewhat longer tail to low column density than the low redshift sub-sample, and we note that low column-density systems are arguably rather more likely to go unrecognized at lower redshifts (discussed further in Section 4.2.2). However, another potential selection effect is that the proportion of dusty sightlines appears to decline with increasing redshift above $z \sim 3$ (Kann et al. 2010; Perley et al. 2016a,b; Zafar et al. 2018a), and if dusty bursts are systematically lost from the low redshift sub-sample, due to the difficulty of locating and obtaining spectra for the afterglows, then it could mask a more significant evolutionary trend. The issue of biases due to dust is one we return to in subsequent sections.

There is a suggestion of a more significant decline in the typical values of $\log(N_{\rm HI})$ at $z \gtrsim 6$ (as also pointed out by Chornock et al. 2014; Melandri et al. 2015), which influences the final $z > 5$ bin (red line). However, the conclusion is still limited by small number statistics, and a KS test again finds this $z > 5$ sub-sample to be consistent with being drawn from the same distribution as the lower redshift ($z < 5$) sub-sample (p value of 0.30).

3.5 Dependence on host properties

In Fig. 3 we plot $\log(N_{\rm HI})$ versus host UV absolute magnitude, $M_{\rm UV}$, which is a gauge of the current (unobscured) star formation rate, for those bursts in our sample where good constraints on host luminosity are available in the literature (37 measurements and 18 upper limits, detailed in Table 1). The restricted number of cases for which deep host searches have been conducted, and the fact that many are upper limits, means we cannot draw firm conclusions, but there is little indication of a dependence of the average HI column density on the current star formation rate. Note, we have converted these values to a common cosmology (a flat Friedmann model with $\Omega_{\rm M} = 0.3$, $H_0 = 70\,{\rm km\,s}^{-1}$), but not otherwise attempted to correct for differences in the procedures used by different authors (approaches to k-corrections, for example), or small deviations from the reference 1600 Å wavelength generally adopted. These distinctions should not be at a level that would affect the conclusion.

Similarly, in Fig. 4 we plot $\log(N_{\rm HI})$ against host stellar mass, M_*, for those galaxies in our sample for which estimates (or limits) are available in the literature (Table 1). The bulk are based on *Spitzer* infrared photometry, particularly from Perley et al. (2013), Perley et al. (2016b), Laskar et al. (2011), and Myers et al. in preparation.
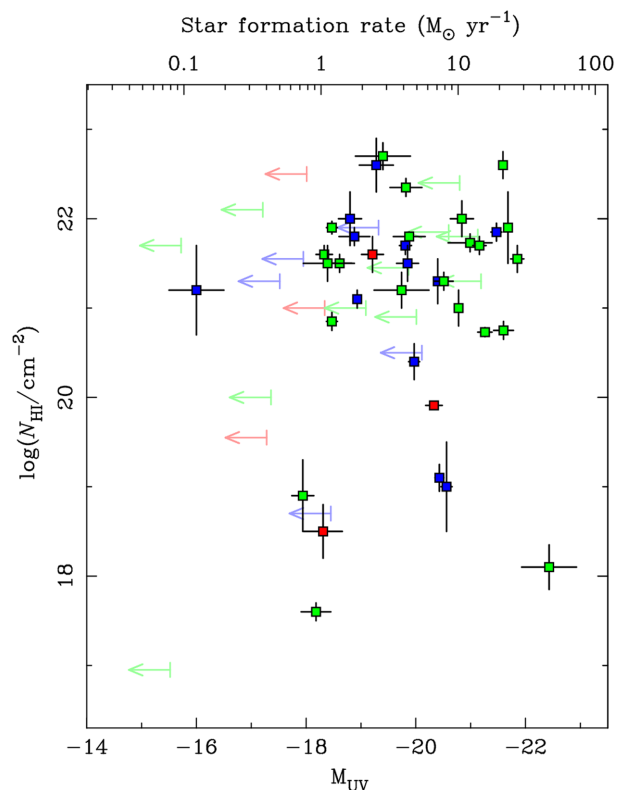
Figure 3. The values of neutral hydrogen column density plotted against host rest-frame UV absolute AB magnitude and corresponding star formation rate (top axis, following the calibration for a $Z = Z_\odot/3$, constant star-formation rate and age >300 Myr population from Madau & Dickinson 2014), for 37 detections and 19 upper limits collected from various sources (Table 1). Colour coding is as with the lines in Fig. 2 and upper limits are 2σ.

Here we are restricted to 28 galaxies with M_* estimates and 31 galaxies with upper limits. Again there is little indication of any trend, contrary to suggestions that $f_{\rm esc}$ may correlate strongly with galaxy size (e.g Anderson et al. 2017).

One trend that is conspicuous in Fig. 3, and in particular Fig. 4, is that the UV brighter and more massive hosts are predominantly in the $3 < z < 5$ bin. It is true that small and faint hosts are harder to detect at higher redshifts, and that may explain some part of this trend. However, another factor seems to be that higher mass ($M_* \gtrsim 10^{10}\,{\rm M}_\odot$) hosts at $z < 3$ are more often associated with heavily extinguished bursts, and hence more likely to be highly dusty, than at higher redshifts (Perley et al. 2016b); these are presumably systematically under-represented in our compilation.

3.6 A high-quality sub-sample

Our full sample consists of bursts spanning a large range of redshift and intrinsic brightness, and were observed with a variety of instruments, exposure times, and times post-burst. The spectra at Lyα therefore range from the very good to poor (see examples in the Appendix), and it is natural to ask whether inclusion of some poor spectra has a significant effect on our results.

To gain some insight into this we selected a high-quality sub-sample by removing bursts that either had poor continuum S/N in the relevant spectral region, had imprecise redshifts (due to lack of metal lines), were affected by instrumental issues such as chip
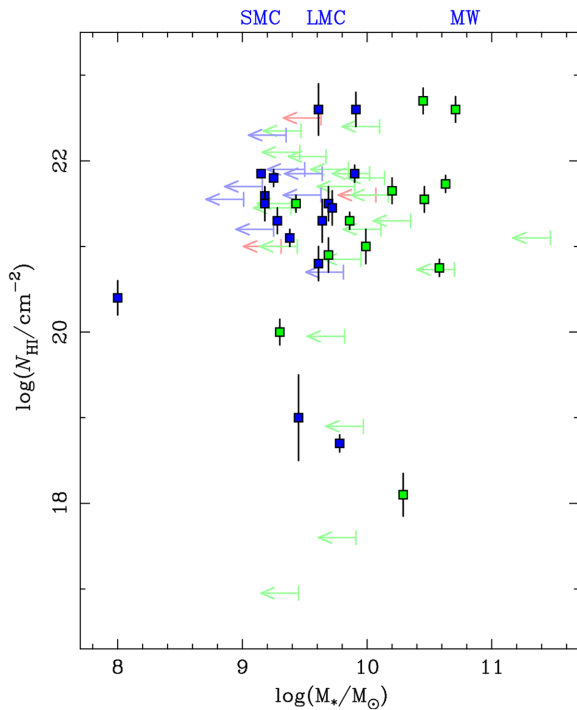
Figure 4. The values of neutral hydrogen column density plotted against host stellar mass estimates from a range of sources (Table 1) for 60 hosts, 32 of which are upper limits (shown at 2σ). Colour coding is as with the lines in Fig. 2. The approximate stellar masses of the Milky Way and Magellanic Clouds are indicated on the top axis for comparison.

gaps, had indications of significant Ly α emission in the absorption trough, or otherwise were not well fit by the damping wing profile. We also removed a small number of cases where $N_{\mathrm{H\,I}}$ values were obtained from the literature, but the original spectra not shown in the papers reporting the results. The bursts surviving this exercise are indicated by asterisks in Table 1.

Analysis of this 96-member 'high-quality' sample results in an average escape fraction of $\langle f_{\mathrm{esc}} \rangle = 0.007$, and, following the same procedure as above, a 98 per cent upper limit of $\langle f_{\mathrm{esc}} \rangle < 0.020$. Broadly, then, the result is very comparable with that for the whole sample; a slightly higher upper limit is unsurprising simply due to the smaller sample size. We caution, however, that some of the potential selection effects described below are likely to be more severe for a sample selected based on the quality of the spectra. For example, high column-density sightlines that also suffer high extinction will be easily lost in such a sample, and conversely those with low column are less likely to exhibit detectable metal lines for redshift determination. Furthermore, given that we are fitting a well-defined damping wing model, even poor quality spectra should yield H I column densities to sufficient precision for the present analysis. For these reasons we regard the full sample as giving the more robust results.

4 POTENTIAL SYSTEMATIC UNCERTAINTIES

A number of systematic uncertainties may affect our analysis, potentially biasing the conclusions. These include observational selection effects: in order to be included in the sample afterglows must be localized and spectra obtained that cover the Ly α region with reasonable signal-to-noise.

Other concerns relate to the still-uncertain nature of the GRB progenitor itself, both in terms of the assumption that their sightlines are representative of dominant EUV-producing stars, and specifically whether there could be special circumstances required to produce GRBs that necessitate an atypical environment. It is also pertinent to ask whether the results can be extrapolated to the EoR.

In this section we begin by investigating systematic effects that may influence our calculation of $\langle f_{\mathrm{esc}} \rangle$ in terms of its application to the GRB progenitors. The majority ($\sim$70 per cent; Gehrels & Razzaque 2013) of *Swift*-discovered GRBs do not have redshifts, which, it may be thought, could lead to large biases. With a more uniformly selected sample, some of these effects might be quantified via simulated data sets, but that approach would be of limited utility here. However, by considering the nature of these selection effects, and surveying the available data, we shall show that these biases can be understood well enough to confirm that they are unlikely to affect the main conclusions.

We then consider more carefully how representative the GRB progenitors are of the EUV-producing massive stars, and the potential systematic uncertainties that may introduce. Finally we discuss in more detail the application of our results to the EoR.

4.1 Systematic overestimation of $\langle f_{\mathrm{esc}} \rangle$

Two factors are very likely to produce an overestimate of the escape fraction, as discussed here.

4.1.1 Dust extinction biases

GRB afterglow surveys are biased against high column-density sightlines since they tend to be dustier and hence harder to locate and obtain redshifts for in the optical band (Fynbo et al. 2009; Greiner et al. 2011; Watson & Jakobsson 2012). Dusty systems at higher redshift would be particularly susceptible to being lost since even near-IR observations will be looking in the source-frame optical or near-UV. However we expect dusty systems to be rarer at $z \gtrsim 4$ (Perley et al. 2016b) and particularly by $z \sim 6$ (cf. Zafar et al. 2011; Schaerer et al. 2015). Recently Bolmer et al. (2018b) have shown that the decline of obscuration in GRB afterglows with increased redshift is likely primarily due to their hosts being less dusty rather than an observational selection effect.

Over all redshifts, Perley et al. (2016a) estimate that approximately 20 per cent of GRBs detected by *Swift* are heavily dust obscured, and often reside in globally dusty, massive galaxies (Rossi et al. 2012; Perley et al. 2013); this subpopulation is significantly biased against in afterglow samples. A similar proportion show signs of more moderate dust obscuration (see also Covino et al. 2013). Thus this effect, while important for understanding the overall GRB host population, would likely only necessitate a comparatively minor correction to the escape fraction estimate (i.e. a $\sim$20–40 per cent reduction, assuming that all very dusty sightlines are opaque to EUV), and the correction is likely to be greatest at $z < 3$, as discussed in Section 3.4.

Even in some cases where afterglows have been detected and redshifts measured, there may be significant attenuation in the UV by dust. However, from the point of view of escape fraction, this is only relevant for the two sightlines with non-negligible f_{esc}, and as already discussed in Section 3.1 may lead to corrections (downwards) of a factor $\sim$2 or more for our sample.

4.1.2 Effects of GRB prompt emission and early afterglow on local gas and dust

The GRB prompt flash and early afterglow produces an intense radiation field that is expected to quickly destroy dust (Waxman & Draine 2000; Morgan et al. 2014) and ionize gas to distances of up to several tens of pc when the ambient medium has a low to moderate density, $n \lesssim 10 \, \text{cm}^{-3}$ (Perna & Lazzati 2002; Vreeswijk et al. 2007; Krongold & Prochaska 2013). Therefore the opacity measured to the afterglow could, in principle, be less than the opacity that would have been seen to the progenitor star system. Various lines of evidence suggest the existence of an ionized gas component, likely reasonably local to the GRB. In particular, it has been argued that high column densities measured in X-ray absorption, which in some afterglows significantly exceed the optical measures, are at least partially due to denser gas close to the progenitor in which the hydrogen has been ionized (Watson et al. 2007; Schady et al. 2011). Furthermore, the observed correlation of X-ray absorption with local galaxy surface brightness (in optically bright GRBs) may support a local origin for a significant proportion of the absorbing gas (Lyman et al. 2017). Highly ionized species have also been seen in some afterglow spectra, which are likely to be of circumburst origin (Fox et al. 2008; De Cia et al. 2011; Heintz et al. 2018).

On the other hand, significant ionization may have been brought about by the stellar radiation field prior to the burst (Krongold & Prochaska 2013; Watson et al. 2013), rendering the ionizing effect of the GRB largely irrelevant. This is supported by models of feedback from star formation in massive molecular clouds that show that hot ionized bubbles can grow to tens or hundreds of pc in a few Myr, although in some circumstances, in particular if star formation is relatively inefficient, the outflow can stall and the cloud recollapse, leading to further star formation episodes (e.g. Rahner et al. 2017).

In principle, deep time-resolved spectroscopy may allow the GRB-driven ionization of H I to be observed directly (Perna & Lazzati 2002), although in practice, sufficiently good data sets have rarely been acquired. Only in one case, namely GRB 090426, has time-variability of Ly α been seen, between spectra obtained at 1.1 and 12 h post-burst, suggesting the influence of the GRB. Here photoionization modelling placed the absorbing gas at ∼80 pc (Thöne et al. 2011). As discussed in Appendix A14, there is uncertainty regarding this particular burst as to whether it is of the long or short duration class, but none the less it confirms that the local ionizing effect of GRB emission can occur even at quite large distances.

In one other case, GRB 080310, Vreeswijk et al. (2013) found that their time-dependent photoionization model to be improved with the addition of a cloud at ∼10–50 pc from the burst, which became fully ionized by the early afterglow emission. The required column density of this cloud, of $\log(N_{\text{HI}}/\text{cm}^{-2}) \sim 19\text{–}20$, was greater than the $\log(N_{\text{HI}}/\text{cm}^{-2}) = 18.7$ inferred for the observed neutral absorber.

In conclusion, it is likely that some fraction of GRBs exhibit a reduced H I column density due to the ionizing effect of the burst itself. If windows to the IGM often occur when superbubbles puncture low-density channels out of galactic neutral gas (e.g. Dove, Shull & Ferrara 2000; Roy, Nath & Sharma 2015), then this may be largely irrelevant as far as high escape fraction sightlines are concerned. On the other hand, regarding our sample, if GRB 060607A was dust extinguished (Section 3.1.2), then it would be surprising if the dust was not associated with some neutral gas that was ionized by the burst.

4.2 Systematic underestimation of $\langle f_{\text{esc}} \rangle$

A reasonable question is whether some very low N_{HI} systems may not have been recognized in GRB afterglow observations. Omitting from our sample, or overestimating the column density, of even a fairly small number of such bursts could lead to significant underestimation of $\langle f_{\text{esc}} \rangle$. There are several circumstances in which this could plausibly arise that are discussed below. The nature of such biases depends on the quality of the afterglow spectroscopy, and so we split our discussion into three broad categories: good S/N spectra (Sections 4.2.2 and 4.2.3), poor S/N spectra that were still sufficient to provide a redshift (Section 4.2.5), and instances where no redshift was obtained due to the faintness of the optical afterglow (Section 4.2.6). These divisions are somewhat qualitative, but this is appropriate given that we do not have access to many individual spectra, and also noting that continuum S/N can vary significantly within a spectrum.

However, first we consider what can be said about the potential level of such selection effects, by reference to a nearly redshift-complete GRB sample.

4.2.1 Lessons from the SHOALS sample

Only a fraction of X-ray localized GRBs have optical/nIR afterglow identifications, and only a fraction of those have redshifts from afterglow spectra.[3] Thus, if the chances of a redshift being obtained depend on the H I column density then it could bias our results. On the other hand, many GRBs receive little ground-based follow-up for other reasons, for example, because of poor weather at major observatories, because they are badly placed for observation due to proximity to the Sun, Moon, or Galactic plane, or simply because of the limited availability of large telescopes to make the necessary rapid target-of-opportunity observations.

Since our sample is not selected or observed in a uniform way, and many values are taken from the literature, it is hard to assess the maximum scale of these effects directly. However, we can get a handle on them by considering the well-defined *Swift* Gamma-Ray Burst Host Galaxy Legacy Survey (SHOALS) sample (Perley et al. 2016a), which consists of 119 long-duration GRBs discovered by *Swift* up until 2012 October, and excludes bursts that were poorly placed for ground observation (whether or not they have redshifts). SHOALS imposes a threshold on the prompt γ-ray fluence of $S_{15-150\,\text{keV}} > 10^{-6} \, \text{erg} \, \text{cm}^{-2}$, which does mean it excludes some intrinsically very weak events, but prompt emission is thought to arise from internal processes within the GRB jet and so not to be dependent on the nature of the ambient environment. Furthermore, despite many searches, there is little indication that prompt γ-ray behaviour depends on other properties of the host, such as metallicity (e.g. Levesque et al. 2010b; Japelj et al. 2016). SHOALS also requires that bursts have identified X-ray counterparts, but since all long-bursts are detectable in X-rays if observed sufficiently early by *Swift*, the selection criterion employed was simply that a rapid autonomous slew was performed. This is consistent with theoretical expectations that the X-ray afterglow flux should be independent of ambient density, n, unless it is very low ($n < 10^{-3} \, \text{cm}^{-3}$, e.g. Hascoët et al. 2011).

---

[3]By way of illustration, to the end of 2017, the data base maintained by Jochen Greiner, http://www.mpe.mpg.de/~jcg/grbgen.html, lists 1200 GRBs with X-ray counterparts and 720 with optical identifications. Of these, 301 have afterglow redshifts according to the data base maintained by Daniel Perley, http://www.astro.caltech.edu/grbox/grbox.php.

The SHOALS sample has a high degree of redshift completeness thanks in large part to major efforts to obtain redshifts from host galaxy observations (identified within X-ray or optical afterglow error boxes) where they had not already been obtained from afterglow spectroscopy. Specifically, 92 per cent have spectroscopic or (in a few cases) good photometric redshifts, and all but one have some photometric constraint on the redshift.

Here we restrict our attention to the 80 bursts for which the redshift is $z > 1.6$ or for which the constraints allow the possibility of the burst being in that range. Of these we can immediately say that 52 were very likely high column-density sightlines, either because N_{HI} was measured directly (39) or because they were found to have faint afterglows with indications of high levels of extinction (14) according to Perley et al. (2016a, see also Section 4.1.1). One, namely GRB 060607A, is the same low-column system included in our sample.

Of the remainder, 19 appear to have had at least moderately bright optical afterglows, but either spectroscopy was obtained that did not cover the wavelength of Ly α (8) and the redshifts rely on metal lines (although in no case were these lines reported as being unusually weak) or simply no spectroscopy was attempted to our knowledge (11). A further four had little afterglow follow-up of any kind reported; these were GRB 050128, early in the *Swift* mission, GRB 050726, for which real-time alerts were not sent to the ground, GRB 050922B that occurred on the same day as several other high-priority bursts, and GRB 070328. We find no reason to think any of these bursts lacked Ly α measurements due to observational selection effects, since they all seem to be cases where only limited follow-up was attempted.

This leaves only three sources, which merit more thorough scrutiny. One of these, GRB 071025, was observed with Keck/HIRES, but the spectrum was low-S/N with flux only being detected at $\lambda > 7500$ Å. Fynbo et al. (2009) argued that this may be due to a Ly α break at $z \approx 5.2$ (the low S/N precluding measurement of the line strength), or alternatively that it could indicate a highly dust reddened afterglow at lower redshift. A photometric redshift constraint from multiband afterglow imaging supports a high redshift ($z \sim 5$) interpretation, whilst also favouring fairly substantial dust extinction (Perley et al. 2010). Thus it seems this is an intrinsically bright event but, again, most likely with a high column-density sightline.

GRB 100305A was the target of several deep imaging observations within the first hour post-burst, but the only candidate afterglow (Gemini/GMOS observations in *riz*; Cucchiara 2010) was subsequently found to be outside the revised X-ray error circle and to be present as a steady source in later imaging (Perley et al. 2016a). We have analysed previously unpublished early UKIRT data, and also find no afterglow down to a 2σ limit of $K_{AB} = 20.7$ at 40 min after the trigger. In fact the *Swift*/XRT spectrum (see http://www.swift.ac.uk/xrt_spectra/00414905/; Evans et al. 2009) does show significant X-ray absorption above the Galactic value, suggesting a high column sightline, possibly combined with moderately high redshift making the optical/nIR afterglow faint.

Finally we have GRB 070223, which is known to be at redshift $z = 1.63$ from the host galaxy (Perley et al. 2016a). Here the afterglow was faint in both the optical and near-infrared, despite early follow-up, meaning that no spectroscopy was attempted. The host galaxy was detected in *Spitzer* 3.6 μm imaging, but the implied stellar mass is a relatively modest $\log(M_*/M_\odot) \approx 9.5$ (Perley et al. 2016b). We have reanalysed the early imaging obtained at the Liverpool Telescope and the WHT at $\approx$3 h post-burst (details are given in Appendix A3), finding AB magnitudes of $r = 23.8 \pm 0.3$ and

$K = 22.0 \pm 0.3$ for a faint source at the X-ray afterglow position. However, we have also analysed the SDSS and PanSTARRS imaging of the same region, and in both cases find a persistent source, presumably the host, at the same location, with a magnitude $r = 23.5 \pm 0.3$. Thus, it seems clear that the optical source seen by the LT (and also the MDM 1.3m; Mirabal, Melandri & Halpern 2007) was actually host dominated, and hence the optical afterglow must have been substantially fainter. By contrast, the K-band source faded by 0.7 mag by the following week, confirming an afterglow detection in the near-IR (Rol et al. 2007). Thus it seems likely that, despite not being in a massive dusty host, this event too was heavily extinguished, which is consistent with the high column density inferred from the X-ray spectrum of $\log(N_{HI,X}/\mathrm{cm}^{-2}) \approx 22.6$ (see http://www.swift.ac.uk/xrt_spectra/00261664/; Evans et al. 2009).

In summary, from our analysis of the SHOALS sample, of 80 bursts that are or may be at $z > 1.6$, 55 have evidence of high-N_{HI} and/or high extinction and one has low column ($\log(N_{HI}) < 18$). In all other cases, limited follow-up seems to be the primary reason for a lack of a constraint on N_{HI}. This is worth emphasizing: even amongst bursts that were chosen as being well-placed for follow-up and which had at least moderately bright afterglows, a significant number of events ($\sim$25 per cent) lack spectroscopic constraints on Ly α absorption for reasons that seem to be unrelated to the afterglow properties. Thus, it seems that the large majority of optically faint bursts are dust extinguished, with a smaller number at high redshift and hence optical 'drop-outs'. The predominant selection effect, then, leads to high-N_{HI} bursts being lost from the sample (already discussed in Section 4.1.1). This suggests that any bursts that are lost from our sample due to selection against low column-density systems must be few in number.

4.2.2 Featureless or very weak-lined GRB afterglow spectra

In rare cases, like GRB 071025 discussed above, afterglow spectra are acquired in which no absorption features can be seen at a reasonable confidence level, or that exhibit only marginal features that cannot be unambiguously identified. This could be due to foreground gas in the host having very low column density such that it produces neither a clear Ly α feature nor detectable metal lines, with the net result that no redshift is obtained. However, in our experience, such apparently featureless spectra are nearly always cases where either the continuum level has very low signal-to-noise (S/N) ratio (as was the case for GRB 071025), thus not necessitating an especially low column density, and/or the spectrum only covers a relatively short wavelength range and so may easily miss prominent absorption features.

Problems associated with low-S/N spectra are discussed in Section 4.2.5. The possibility that intrinsically fainter afterglows, which typically result in no afterglow redshift being determined, may on average have low column-density absorbers, we return to in Section 4.2.6. Here we restrict attention to whether weak absorption features could have led to no redshift being found despite the spectra being of moderate to good S/N and spanning a wide wavelength range.

Again, our experience suggests that such circumstances are very rare: we are not aware of any compelling examples, published or unpublished. A much discussed near-miss was GRB 070125, for which the absorption lines were very weak, but ultimately the redshift was found to be $z = 1.55$ from Mg II absorption seen in a Gemini/GMOS spectrum (Cenko et al. 2008). A later Keck/LRIS spectrum of the afterglow, which extended to shorter wavelengths,

showed marginal evidence for Lyα absorption, but this was only sufficient to conclude $\log(N_{HI}/\text{cm}^{-2}) < 20.3$ in the host (Updike et al. 2008). Based on the weakness of the metal lines, De Cia et al. (2011) argued that the neutral hydrogen column density was probably low, likely in the LLS range, but that this could have been substantially diminished by the particularly intense afterglow radiation ionizing gas to a considerable distance. Given that Lyα was so far into the near-UV in this case, around 3100 Å, which is hard to calibrate in ground-based data, we did not include it in our sample. The unusual nature of this system is illustrated by the fact that GRB 070125 had the lowest 'line-strength-parameter' (an index based on the strength of absorption lines compared to the average over the sample) out of 69 spectra studied by de Ugarte Postigo et al. (2012).

Another instructive case is GRB 140928A, for which spectroscopy was obtained with Gemini/GMOS-S (Cucchiara, Cenko & Perley 2014). Here the afterglow continuum was clearly detected, but no unambiguous lines were seen, despite the S/N being moderately good (S/N $\approx$ 8 per spectral resolution element at 6500 Å). In this case the spectral range was 5680–10 250 Å, with two 80 Å chip gaps; thus it is plausible that simply no intrinsically strong lines happened to lie within this window. What we can say, though, is that for Lyα to fall within the spectrum would have required $z > 3.7$, which would mean we would have expected a clear break due to the onset of the Lyα forest, irrespective of the host column density. This is not seen, so we can conclude that Lyα very likely was not within the spectral window in this case.

Thus, this example highlights an important point regarding weak-lined spectra, namely that at least above redshift $z \sim 3$ strong attenuation due to the Lyα forest would normally be expected to be clearly seen in reasonable S/N optical spectra covering the relevant wavelength range, giving good indications of the redshift, even in the absence of any host absorption.

Finally we note that, while there have been occasional instances when host galaxy follow-up has revealed an earlier claimed afterglow redshift (based on a low-S/N spectrum) to be mistaken (e.g. Jakobsson et al. 2012), to our knowledge none of these have indicated a case where the afterglow spectrum should have revealed Lyα absorption that was not seen. All these considerations suggest that any bias introduced by the effect of low host column density going unrecognized despite good afterglow spectroscopy should be minor compared to the other effects we consider.

4.2.3 Mis-measuring low column-density systems

A more subtle question is whether N_{HI} values may be overestimated simply due to the measurement process, particularly for low-S/N spectra. This should not be a major concern in the majority of cases, where damping wings are clearly seen and fitted, confirming the high column density. For cases with rest-frame equivalent width of Lyα less than $W_0 \sim 5$ Å (roughly $\log(N_{HI}/\text{cm}^{-2}) \sim 19.5$), especially when observed at low spectral resolution (typically $R \lesssim 2000$), uncertainty in the velocity structure of the absorbing gas leads to relatively high uncertainty in the inferred H I column density. If the range in velocity of the absorbing gas is underestimated, for example, if due to several clouds with different velocities, then it would lead to an overestimate of the column density.

Of our sample, three bursts both fall into this category and lack direct evidence of emission or otherwise below the Lyman limit, namely GRBs 060124, 060605, and 090426. The last of these was unusual in exhibiting apparent variability of Lyα absorption

(Appendix A14), suggesting absorption dominated by a single absorber. The other two are more difficult cases, although the spectral resolution is sufficient to rule out a high spread in velocity (cf. GRB 021004, Appendix A1), and the inferred H I columns (and error bars) appear to have considered a fairly conservative range of Doppler parameters, making a significant overestimate unlikely.

4.2.4 Mis-identification of the host absorber

A similar possible scenario involving very low column density would be where the host absorption lines were not identified in the spectrum at all, but instead chance alignment with a stronger intervening absorption system led to the incorrect assignation of its redshift as the redshift of the burst, along with an erroneous column density. Again, this is likely to be a rare circumstance since the incidence of strong intervening absorbers is not high and one would normally expect to see the Lyα forest from the IGM, particularly above $z \sim 3$, which would allow identification of an unassociated Lyα absorber as being due to an intervening system. We also note that in some spectra we detect metal fine-structure lines, which are thought to be the result of excitation by the burst itself of gas within its host galaxy, confirming the association (e.g. Vreeswijk et al. 2006).

A particular example that highlighted this concern was GRB 071003, in which it was found that the highest redshift system, a detection of Mg II, presumed to be from the host, was notably weaker than some intervening absorbers (Perley et al. 2008). Similarly, GRB 060605 exhibited weak Lyα from the host, but stronger ($\log(N_{HI}/\text{cm}^{-2}) = 20.9$) from an intervening system at slightly lower redshift (Ferrero et al. 2009).

Another pertinent case is GRB 141026A, the afterglow of which was observed by GTC, with a spectrum covering the wavelength range 5100–9800 Å. The S/N was rather poor, but an absorption line was seen close to the blue end of the spectrum that if interpreted as Lyα would imply $z = 3.35$ and a low column density of $\log(N_{HI}/\text{cm}^{-2}) \lesssim 20$ (de Ugarte Postigo et al. 2014b). In this instance, there were no other features seen to confirm the line identification, and no evidence of a decrement that could be ascribed to the Lyα forest, for which reasons we chose not to include this burst in our sample. Thus, this example illustrates that misidentification of redshift might in some circumstances result in a bias in the opposite direction, namely towards lower column density.

Once again, we conclude that whilst it is hard to rule out completely, the rate of strong intervening absorbers being falsely identified as host systems, providing good spectra are obtained, must be very low.

4.2.5 Low signal-to-noise spectra

Some afterglow spectra are sufficient to provide redshifts, but the signal-to-noise, at least around the Lyα region, is poor. This may lead to N_{HI} being undetermined, particularly if it is low, thus creating a bias in favour of including higher column-density systems. Amongst our sample, only 11 bursts lack clear metal line detections, and of these six have tentative metal line and/or Lyβ detections (GRBs 020124, 060927, 080129, 080913, 081203, and 121229A), and five have no metal line detections but do show an unambiguous continuum break at Lyα that is sufficiently well defined to constrain the wing profile (GRBs 060522, 090519, 100316A, 130427B, and 140515A). The latter subset all have low S/N, and the search for metal lines was complicated by low spectral resolution and/or being

in a difficult region of the spectrum, but reassuringly they span a wide range of N_{HI} values, which is not suggestive of any particular bias. This gives confidence that our sample derives predominantly from high-S/N spectra, and contains few bursts that are only included because they had a particularly high value of H I column density.

Several other bursts have a redshift determined from the Lyα break, but the S/N proved insufficient to estimate the N_{HI} value. These cases are few in number: apart from several at $z \gtrsim 6$, from a search of spectra we have ourselves and the literature we have only identified GRBs 071025 ($z \approx 5$; Section 4.2.1), 140428A ($z \approx 4.7$; Perley 2014), and 160327A ($z \approx 5$; de Ugarte Postigo et al. 2016). Thus we believe that these cases, while they may be below the median N_{HI} for all bursts, are not likely to be unusually low N_{HI}. A small bias could partially offset the bias against dusty sightlines discussed previously.

It is notable that redshifts can be obtained from low-S/N spectra when the redshift is comparatively high, which can be understood because the strength of the Lyα break increases with redshift. At redshifts below $z \sim 3$ such spectra likely will not yield secure redshifts, a category that is discussed in the next section.

4.2.6 When redshifts are not obtained: could GRBs in low-density environments have intrinsically fainter afterglows?

We have argued in the preceding sections that bursts are unlikely to have been lost from our sample due to weak absorption lines providing that good spectra were obtained. However, bursts with very faint optical afterglows will be under-represented due to the increased difficulty of arcsecond localization and redshift determination (either because spectroscopy was not attempted, or because spectra had too low S/N to give a conclusive redshift or N_{HI} measure). Thus, if bursts occurring in low-density environments had weaker lines and also on average fainter afterglows, then that potentially may lead us to systematically lose bursts with high f_{esc}. One way a GRB progenitor could find itself in a lower density environment, would be if it was formed by a so-called 'runaway' star. We consider this particular issue in Section 4.4, but here focus on the potential effect of low density on the brightness of afterglows and the likelihood that such systems have been missed.

As discussed above, the majority of optically faint afterglows are dust extinguished, and have high EUV opacities, while a smaller number are high redshift optical drop-outs. We should also remember that some afterglows were faint when observed simply due to the delay in acquiring spectroscopy. This suggests that the fraction of systems that are faint due to low-density circumburst media is low. On the other hand, basic synchrotron afterglow theory provides some motivation for thinking that such a trend might occur. In particular, for a relativistic jet shocking a medium of uniform density, n, in typical circumstances the optical afterglow flux should scale with $n^{1/2}$ (Granot & Sari 2002). In fact, with sufficiently good wide-band monitoring of the afterglow, the ambient density of the medium in which the jet is travelling (i.e. sub-pc scales) can be calculated. The range of circumburst medium densities inferred from such modelling is quite wide, from 10^{-4} to 10^3 cm^{-3} (e.g. Laskar et al. 2014), but equally is subject to model assumptions and large uncertainties in many cases.

However, the crucial point is that the density structure of the immediate circumburst environment is likely determined by the recent mass-loss history of the progenitor system, and potentially that of any companions (van Marle et al. 2006, 2008). This is very un-

likely to be correlated with the density of neutral gas producing the Lyα absorption, which is generally situated at significant distances of at least tens and often hundreds of pc from the burst site (e.g. Prochaska, Chen & Bloom 2006; Vreeswijk et al. 2013).

From an empirical point of view, there are few indications of any correlations of afterglow intrinsic luminosity with other host properties, including column density. For example, de Ugarte Postigo et al. (2012) found no evidence of a correlation of afterglow luminosity at the time of observation with the observed line strength in a sample of 69 bursts. In fact, some low column-density systems actually have notably bright optical afterglows, including, as mentioned in Section 3.1.2, GRB 060607A, which has the lowest value of N_{HI} in our sample. Other low column-density GRBs with bright afterglows (given the time post-burst they were first observed) were GRBs 070125 ($V = 18.5$ at 13 h post-burst Updike et al. 2008), 071003 ($R = 12.8$ at 42 s post-burst Perley et al. 2008), and 140928A ($r = 20.8$ at 22 h post-burst Varela et al. 2014), all discussed above. To some extent this could be regarded as a selection effect, since weak lines can only be detected, or even searched for, in high-S/N spectra. It is also the case that one expects GRBs with highly luminous optical flashes to be more effective at ionizing gas to larger distances (Section 4.1.2). However, this does at least indicate a large scatter in any putative correlation of intrinsic afterglow luminosity and Lyα strength, and combined with the comparative dearth of featureless afterglow spectra (Section 4.2.2), leads us to conclude that any such bias must be small.

4.3 How representative are GRB progenitors of the dominant stellar sources of EUV radiation?

An essential assumption in our analysis is that GRBs are good tracers of the locations of populations of massive stars likely to be responsible for the bulk of EUV radiation production. In this section we discuss the extent to which this is true, and consider the potential implications for our results.

4.3.1 Metallicity effects

GRBs preferentially occur in low (sub-solar) metallicity environments (Krühler et al. 2015; Japelj et al. 2016; Perley et al. 2016b; Graham & Fruchter 2017; Vergani et al. 2017), which are typically (but not solely) in less dusty and smaller galaxies (e.g. Schulze et al. 2015; Blanchard, Berger & Fong 2016), and therefore might be expected to have lower neutral gas column densities (although see e.g. Gnedin, Kravtsov & Chen 2008; Sharma et al. 2016, for counter arguments). Lower metallicity populations also produce more EUV for a given star formation rate (Stanway et al. 2016). These factors may result in an overestimate of the escape fraction averaged over all galaxies at lower redshifts, but at higher redshifts (above $z \sim 4$) we would expect low metallicity to be the dominant mode of star formation, and for it to be increasingly occurring in small galaxies (we return to this issue in Section 4.5).

4.3.2 Time-scales of EUV emission compared to GRB progenitor lifetimes

GRB positions are well correlated spatially with regions of high mid- and near-UV emission in their hosts, and specifically more highly correlated than are most (type II) core-collapse supernovae (Fruchter et al. 2006; Svensson et al. 2010; Blanchard et al. 2016). This has previously been used to argue that if the GRB progenitor is
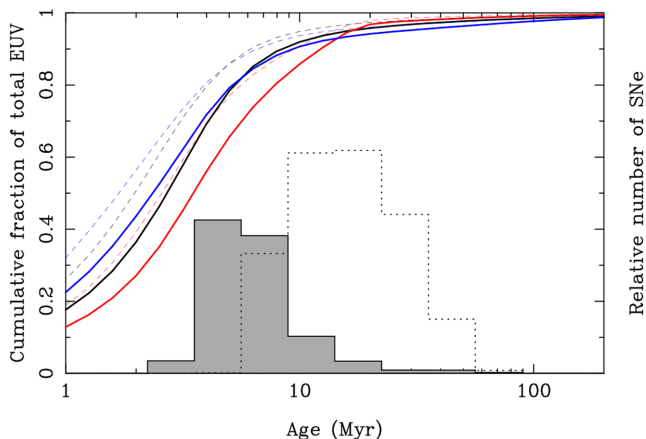
Figure 5. Output of EUV radiation for a single burst of star formation as a function of age from the BPASS models, which include prescriptions for binary stellar evolution (Eldridge & Stanway 2009). Shown are three models, 0.1 $Z_\odot$ (red), 0.3 $Z_\odot$ (black), $Z_\odot$ (blue), for a stellar initial mass function of power-law slope $\alpha = -1.3$ between 0.1 and 0.5 $M_\odot$ and slope $\alpha = -2.35$ from 0.5 to 100 $M_\odot$. Dashed lines are the equivalent models with an IMF going up to 300 $M_\odot$. Also shown for the 0.3 $Z_\odot$ model are the relative numbers of type Ic supernovae (shaded histogram), and type II supernovae (dotted histogram) in each logarithmic age bin.

a single star, it is likely to have initial mass $M > 20$–25 $M_\odot$ (Larsson et al. 2007; Anderson et al. 2012), but in any case, whether single or binary, it suggests average lifetimes less than those of more common core-collapse supernovae.

We can investigate this question more quantitatively using stellar population synthesis models. Specifically, we consider the BPASS models of Eldridge & Stanway (2009). These include prescriptions for the contribution of binary stars, which is essential given the importance of binary interactions to the evolution of massive stars (Sana et al. 2012). In fact binaries both enhance the total EUV output for a given stellar mass and extend the emission in time. This will increase the total number of ionizing photons produced and also the effectiveness of feedback, tipping the balance of ionization versus recombination in the environs of newly formed stars and allowing a greater period for the gas to be cleared. The net result is an increase of up to factors of several in the predicted escape fraction (Ma et al. 2016; Stanway et al. 2016)

In Fig. 5 we show the cumulative EUV production for a single burst population as a function of time for a range of metallicities. A single burst of star formation represents one extreme: if, as is quite plausible, star formation is more continuous in a region of a galaxy (cf. Ochsendorf et al. 2017), then GRBs will also be spread over time and their locations will naturally be more representative of the EUV production sites. The figure shows that the large bulk ($\gtrsim$80 per cent) of such radiation is still produced in the first 10 Myr, in other words, during the lifetimes of all but the most massive stars. Comparatively little EUV is produced after an age of ~10 Myr (cf. Ma et al. 2016), so even if older stars are less deeply embedded in their nascent gas clouds (e.g. through having moved from their birth sites and/or there being more time for stellar feedback, and in particular the accumulated action of supernovae, to carve low-density channels through the neutral gas in their vicinity), they can contribute rather little to the total ionizing radiation output. A caveat is that binary interaction, particularly at low metallicity, may result in envelope stripping of rather less massive stars (~12 $M_\odot$), which may then emit ionizing radiation over a longer period of time (~20 Myr), so

could make a significant contribution to the total EUV output that has generally been neglected to-date (Götberg, de Mink & Groh 2017).

Although the nature of GRB progenitors remains uncertain, most scenarios suggest they are indeed likely to have lifetimes of the order of 5–10 Myr. For example, this is indicated by their correlation with regions of high UV emission (Larsson et al. 2007), and is roughly the range spanned by the viable single star chemically homogeneous evolution models studied by Yoon, Langer & Norman (2006). To place this in context, the relative numbers of type Ic supernovae in logarithmic bins are also shown on Fig. 5, and are predominantly in the range of 3–15 Myr. Since the supernovae accompanying long-duration GRBs are also stripped-envelope events (Hjorth & Bloom 2012), and correlate with the UV light of their hosts in a similar way (Kelly, Kirshner & Pahre 2008), it is reasonable to suppose that they span a comparable range of ages at explosion.

4.4 How representative are GRB progenitors of sources of escaping EUV radiation?

Even if GRB locations are good tracers of the dominant sources of stellar EUV radiation, it might be that they under-represent the stars from which the bulk of the *escaping* radiation is produced. Here we consider several such scenarios.

4.4.1 Time-scales revisited - might GRBs not sample peak periods of transparency?

In Section 4.3.2 we argued that GRBs likely do explode on time-scales relevant for a significant proportion of EUV emission from a single age stellar population. However, if the peak episodes of EUV escape generally occur before the first GRBs explode following a burst of star formation, it is plausible that we may not sample the relevant periods (again, for star formation of a more continuous nature, this will not be a concern).

Modelling in detail the escape of ionizing radiation from young massive stars in a range of realistic scenarios is highly challenging. On the scales of individual clouds outward pressure created by winds, radiation, and supernovae competes with gravitational infall, while ionization competes with recombination. These clouds also vary in size and shape, and have complex turbulent internal structure and magnetic fields. It is also essential to incorporate the processes of star formation and evolution, which introduces further uncertainties. Finally the star forming regions exist in larger scale galactic environments. In order to escape a galaxy, radiation must first escape its local environment, likely the molecular cloud in which the stars formed, and subsequently leak out through the larger scale neutral gas distribution. Here we consider the lessons from recent state-of-the-art models that focus on different aspects of the problem.

Howard et al. (2018) examined the escape of EUV radiation from a range of massive (10^4–10^6 $M_\odot$) giant molecular clouds (GMCs) containing multiple massive star clusters, based on 3D simulations with ongoing star formation. They found the EUV escape from the clouds themselves to be variable in time, with occasional peaks above 10 per cent from 2 Myr after the onset of star formation. The lower mass clouds tend to achieve high escape fractions of 20–100 per cent by ~5 Myr, due to near-complete ionization of the clouds. This is within the time-frame that some GRBs likely occur, even if the bulk of progenitors have longer lifetimes (Section 4.3.2). The intermittency here is partly the result of small-scale density

structure due to the turbulent nature of the cloud, which produces time-changing local density field around the clusters (see also Safarzadeh & Scannapieco 2016). This results in a very anisotropic directional distribution of escaping radiation (something also seen in 3D models of small molecular clouds dominated by a single O star, by Walch et al. 2012). Placing these clouds into a galactic context produces galaxies with rapid (10–20 Myr) fluctuations in SFR and f_{esc}, particularly in dwarf galaxies, with a general trend of stronger episodes of star formation being associated with lower f_{esc}. However, these simulations did not include the effects of winds or supernovae, and also use single star stellar population prescriptions. As noted previously, inclusion of binaries is likely to increase the effectiveness of feedback, and extend the time-scales.

Rahner et al. (2017) performed 1D spherically symmetric calculations, including winds, radiative transfer, and the effects of supernovae, covering a range of cloud masses, densities, star-formation efficiencies, and metallicities. Here absorption is dominated by neutral gas in the swept up shell of material surrounding the central low-density ionized bubble. In those models that show any appreciable EUV escape from the birth cloud at all, they also generally find that a high proportion occurs during the first 2–6 Myr. Of course, these calculations are not able to include anisotropies in the shell structure, which may be key to understanding the escape fraction and, again, presumably star formation and/or EUV production more extended in time would modify these results.

Simulations that place star formation in a more cosmological context, while reliant on less sophisticated prescriptions for the feedback physics, have tended to find episodes of high escape fraction, at least in early galaxies, to have scale times of 10–20 Myr (e.g. Kimm & Cen 2014; Wise et al. 2014; Ma et al. 2016; Trebitsch et al. 2017). This reflects time-scales of star formation activity and consequent supernova feedback that has the dominant effect on the galactic scale gas distribution. Interestingly, Toy et al. (2016) suggested that GRB hosts likely have had episodic star formation, based on comparison of enrichment time-scales with observed metallicities.

For comparison, star formation in the 30 Doradus H II region (the Tarantula Nebula) in the Large Magellanic Cloud, often regarded as a local prototype of low-metallicity star-forming regions that may have been highly abundant in the early Universe, has been occurring in different clumps and clusters for at least ~10 Myr (Sabbi et al. 2016). Inferring the EUV escape fraction from the Tarantula Nebula region is subject to large uncertainties, but a recent detailed study of its massive star population constrained it to be in the range 0–0.6, with a preferred value of 0.06 (Doran et al. 2013).

Clearly this is a field where much work remains to be done. It is plausible that in some circumstances, a burst of star formation in a molecular cloud towards the edge of its galaxy may lead to a brief period of high EUV escape to the IGM before the first supernovae explode. However, it does not seem likely that this could be a common occurrence, and that to produce high average escape fractions would require the combined feedback effects of radiation, winds, and supernovae to disperse and ionize both local and global gas, on time-scales comparable to GRB progenitor lifetimes.

4.4.2 Could GRB progenitors preferentially form in higher density environments?

It has been suggested that GRBs may favour not only low metallicity, but possibly also high density sites (e.g. Kelly et al. 2014; Perley et al. 2015), for example, due to dynamical processes in young dense

stellar clusters being important in the formation of their progenitors (van den Heuvel & Portegies Zwart 2013).

However, even if this is true, it is not obvious that it would significantly affect our conclusions. Very massive and dense clouds are likely to recollapse without dispersal (Rahner et al. 2017), and would also be much less affected by the GRB event itself, so that GRBs forming preferentially in such environments seems to contradict the observation that only a minority of bursts are heavily dust obscured, and that absorption often is predominantly at large distances. Cases of massive GMCs where feedback does drive a strong outflow might, in fact, provide the best chances of creating windows of low-density ionized gas to the IGM, thus favouring low column-density systems. In any event, it remains the case that GRBs occur in a range of environments, based on their galactic locations and the evidence we have of the local density, which all suggests little bias compared to the stars we expect to dominate the escaping EUV radiation.

4.4.3 Could GRB progenitors preferentially remain in higher density environments?

A sizeable fraction (~30 per cent) of OB stars in the Milky Way are found to have sufficiently high space velocities (several 10s of km s^{-1}), presumably as a result of dynamical interactions, that they will end their lives well outside their nascent birth clouds (e.g. Tetzlaff, Neuhäuser & Hohle 2011). Such runaway stars may sometimes spend much of their lives in relatively low-density regions, and so could have a higher $\langle f_{esc} \rangle$ than stars that remain close to their birth sites. If for some reason, such as a requirement to be a binary system, GRB progenitors were less likely to be runaways, then, on the face of it, sightlines to GRBs would not sample that population. On the other hand, since GRBs themselves ionize gas in their locality to significant distance (see Section 4.1.2), and given that including runaways in hydrodynamic simulations only results in a modest increase of $\langle f_{esc} \rangle$ of ~20 per cent (Kimm & Cen 2014), missing runaways are unlikely to have a large effect on our conclusions.

4.4.4 Could GRB progenitors create higher density sightlines?

We can ask whether the special nature of the GRB progenitor may influence the column densities we measure. In particular, to allow a GRB jet to reach highly relativistic velocities, it is thought that their progenitors must have no extended envelope. Indeed, the lack of hydrogen and helium in the spectra of supernovae accompanying GRBs confirms this picture. Expelling the envelope without also losing significant angular momentum is a potential problem for the collapsar scenario for GRB production (e.g. Detmers et al. 2008). One possibility is that high rotation could lead to chemically homogeneous evolution, essentially consuming the envelope (Yoon & Langer 2005). Alternatively, the hydrogen and helium layers might be lost, for example, through explosive common-envelope ejection in a tight binary (Podsiadlowski et al. 2010). In such cases it is plausible that the expelled material, which could amount to ~10 M$_\odot$, might provide enhanced absorption if it remains close enough to provide a significant column density, but far enough not to be ionized by the ambient UV radiation field prior to the burst. Thus, even though large column densities generally seem to be produced by gas at relatively large distance from the GRB site, it could be that a modest contribution from gas at 10–20 pc expelled by the progenitor

sets an effective floor to the distribution of $\log(N_{HI}/cm^{-2}) \sim 17.5$–18 in the GRB sample. Other massive stars that did not produce such high mass-loss would therefore have higher escape fractions.

However, this ignores the ionizing flux of the optical flash and early afterglow of the GRBs themselves. In cases such as the two lowest column-density systems in our sample, GRBs 050908 and 060607A (Section 3.1), the bright afterglows exceeded the flux required to ionize this mass of local gas by orders of magnitude. Only if the peak UV luminosity of the burst was at least as faint as $M_{AB} \approx -22$ could a proportion of the expelled gas remain neutral, and even at $z \approx 2$ this translates to a peak apparent magnitude of $m_V \approx 23$, which is effectively unfeasible for follow-up spectroscopy with reasonable S/N, given the current technology. Thus, excess absorption from gas expelled by GRB progenitors can have no effect on our sample of N_{HI} measurements.

4.5 Applicability to the era of reionization

As already discussed, GRBs favour low-metallicity environments, and in particular appear to have a roughly constant efficiency of occurrence up to around 0.3–1 times Solar metallicity, with a rapid drop above that threshold (Cucchiara et al. 2015; Perley et al. 2016b; Graham & Fruchter 2017; Vergani et al. 2017). This certainly suggests that GRBs should form during the EoR when few galaxies were highly metal enriched. Furthermore, known GRB hosts span a wide range in stellar mass (Perley et al. 2016b), including small, low-metallicity galaxies likely representative of the galaxy populations predominant in the EoR. In particular, while three GRB hosts have now been detected by the *Hubble Space Telescope* (*HST*) at $z \sim 6$ with properties similar to those of Lyman-break galaxies at the same redshift (McGuire et al. 2016), it remains the case that the majority of GRB hosts at $z > 6$ appear to be undetected to *HST* limits, consistent with them being drawn from a galaxy luminosity function in which the faint end dominates (Tanvir et al. 2012a; Trenti, Perna & Jimenez 2015).

Further evidence that GRBs effectively sample stellar populations predominant in the EoR is that the rate of GRBs relative to total star formation appears to rise with redshift even faster than expected due to the metallicity sensitivity already discussed (Kistler et al. 2009; Robertson & Ellis 2012; Perley et al. 2016b), although number statistics are small at the highest redshifts.

Thus to the extent to which analogues of EoR galaxies exist at lower redshifts, we would expect them to appear in the GRB host samples, and to be included in our column-density sample. As discussed in Section 3.3, the high-resolution cosmological simulations of galaxies at $z \sim 7$ of Cen & Kimm (2014) find that roughly half of GRBs should have $\log(N_{HI}/cm^{-2}) < 18$, which we certainly do not see at lower redshifts. If the prediction is correct – and limited statistics rule out a strong test at this stage – then it would require that there is a large sub-population of high-f_{esc} hosts at $z > 6$ that barely exist in the $z < 5$ host sample.

5 DISCUSSION AND CONCLUSIONS

We have compiled a large sample of H I column-density measurements obtained from GRB afterglow spectroscopy. Because GRBs select hosts over a very broad range of luminosity, we consider that they provide a good representation of the dominant populations of (not highly dusty) star-forming galaxies at $z \gtrsim 2$. Despite uncertainties about the exact nature of the GRB progenitor, we also argue that the lifetimes and locations of GRB progenitors likely make them

well suited to sampling the periods of high EUV production, and in particular the peak episodes for its escape.

Out of 140, only two sightlines have sufficiently low column-density to allow any significant EUV to emerge. Assuming this sample is representative of the sightlines to the massive stars dominating ionizing radiation production, we conclude an average escape fraction at the Lyman limit of $\langle f_{esc} \rangle \approx 0.005$, with a 98 per cent confidence upper limit of $\langle f_{esc} \rangle \approx 0.015$. This value is in reasonable agreement with the $\langle f_{esc} \rangle \sim 0.01$ predicted for GRB sightlines based on the hydrodynamic simulations of Pontzen et al. (2010). It suggests that only in rare cases does stellar feedback puncture holes out of the dense ISM, providing clear windows to the IGM. This is a more stringent limit than was obtained from the direct search for escaping EUV at $z \approx 3.3$ by Grazian et al. (2017), who found $\langle f_{esc} \rangle < 0.017$ (67 per cent confidence) for galaxies brighter than L_{UV}^* and $\langle f_{esc} \rangle \lesssim 0.1$ for a sample brighter than $0.2L_{UV}^*$. Furthermore, it is significantly less than the $\langle f_{esc} \rangle = 0.09 \pm 0.01$ found by Steidel et al. (2018) for a sample of $z \sim 3$ star-forming galaxies with $0.2 < L_{UV}^* < 3$.

If we account for the additional opacity due to dust for the two sightlines for which there is any appreciable escape fraction, and the loss of highly dusty bursts from the sample altogether, then these numbers could reduce by factors of 2–3. If radiation from the GRBs themselves ionized some gas in these two high-f_{esc} cases, then the estimate of $\langle f_{esc} \rangle$ should be reduced further.

On the other side of the balance sheet, the difficulty of finding low column-density systems in spectra with poor signal-to-noise does provide a modest selection effect in the opposite direction. However, inspection of more complete sub-samples suggests that even missing one or two cases would be surprising, so the net effect is unlikely to be more than a factor ~ 2 increase in our estimate of $\langle f_{esc} \rangle$.

The bulk of the events are at redshifts $z = 2$–5, which, even accounting for these systematic uncertainties, indicates that stellar EUV falls short of providing the radiation field needed to explain the properties of the Ly α forest in this redshift range (Becker & Bolton 2013; Stanway et al. 2016). More crucially, if their properties apply to galaxies during the EoR, these limits on $\langle f_{esc} \rangle$ are at least an order of magnitude below what is required to maintain an ionized IGM in that era (Robertson et al. 2015; Stanway et al. 2016).

There is a weak suggestion of a decline in average H I column density at the highest redshifts ($z \gtrsim 6$), but statistics remain too poor for definitive conclusions, and none of the $z > 5$ sightlines have an appreciable escape fraction. Furthermore, there is no indication of a strong correlation of neutral hydrogen column density with either galaxy UV luminosity or stellar mass, for the subsets of our sample for which these measures are available. Thus we find no evidence to support the suggestion that ionizing escape fraction may be much higher for the small galaxies that likely dominated star formation in the EoR.

Avoiding this conclusion would seem to require either that GRBs are not good tracers of the primary sources of escaping EUV, for instance, because the large majority occurs before GRBs explode or because there are classes of older and less-massive stars that produce substantially more EUV than has hitherto been appreciated (e.g. as a result of binary interactions; Götberg et al. 2017), or that there is very marked evolution in the properties of GRB sightlines between $z \sim 7$ and $z \sim 2$–5.

Overall this work shows the power of GRBs to address the difficult question of the Lyman continuum escape fraction averaged over the dominant populations of high-redshift star-forming galaxies, and demonstrates the benefits of long-term campaigns to obtain

GRB afterglow spectroscopy. The evidence that GRBs occur preferentially in low-metallicity systems, and that their rate relative to the star formation rate increases with redshift, all suggest that they are likely good tracers of star formation in the EoR. Future samples of larger numbers of $z > 6$ GRBs with good H I column-density determinations may benefit soon from the availability of *JWST*, and in the 2020s through the *SVOM* satellite working in conjunction with follow-up spectroscopy on 30-m class ground-based telescopes. Hence we may hope to obtain much tighter and more direct constraints on the contribution of stars to reionization (Yuan et al. 2016).

REFERENCES

Anderson L., Governato F., Karcher M., Quinn T., Wadsley J., 2017, MNRAS, 468, 4077

Anderson J. P., Habergham S. M., James P. A., Hamuy M., 2012, MNRAS, 424, 1372

Becker G. D., Bolton J. S., 2013, MNRAS, 436, 1023

Berger E., Penprase B. E., Cenko S. B., Kulkarni S. R., Fox D. B., Steidel C. C., Reddy N. A., 2006, ApJ, 642, 979

Blanchard P. K., Berger E., Fong W.- fai ., 2016, ApJ, 817, 144

Bolmer J. et al., 2018a, preprint (arXiv:1810.06403)

Bolmer J., Greiner J., Krühler T., Schady P., Ledoux C., Tanvir N. R., Levan A. J., 2018b, A&A, 609, A62

Bouchet P., Lequeux J., Maurice E., Prevot L., Prevot-Burnichon M. L., 1985, A&A, 149, 330

Bouwens R. J. et al., 2012, ApJ, 752, L5

Camps-Fariña A., Zaragoza-Cardiel J., Beckman J. E., Font J., Velázquez P. F., Rodríguez-González A., Rosado M., 2017, MNRAS, 468, 4134

Castro-Tirado A. J. et al., 2010, A&A, 517, A61

Castro-Tirado A. J. et al., 2014, GCN Circ., No. 16505

Castro-Tirado A. J. et al., 2016, GCN Circ., No. 19632

Cen R., Kimm T., 2014, ApJ, 794, 50

Cenko S. B. et al., 2008, ApJ, 677, 441

Cenko S. B., Berger E., Djorgovski S. G., Mahabal A. A., Fox D. B., 2006, GCN Circ., No. 5155

Cenko S. B., Perley D. A., Morgan A. N., Klein C. R., Bloom J. S., Butler N. R., Cobb B. E., 2010, GCN Circ., No. 10752

Chary R., Berger E., Cowie L., 2007, ApJ, 671, 272

Chen H.-W. et al., 2009, ApJ, 691, 152

Chen H.-W., Prochaska J. X., Gnedin N. Y., 2007, ApJ, 667, L125

Chornock R., Perley D. A., Cenko S. B., Bloom J. S., Cobb B., Prochaska J. X., 2009a, GCN Circ., No. 8994

Chornock R., Perley D. A., Cobb B. E., 2009b, GCN Circ., No. 10100

Chornock R., Cucchiara A., Fox D., Berger E., 2010, GCN Circ., No. 10466

Chornock R., Berger E., Fox D. B., Fong W., Laskar T., Roth K. C., 2014, preprint(arXiv1405.7400)

Christensen L., Fynbo J. P. U., Prochaska J. X., Thöne C. C., de Ugarte Postigo A., Jakobsson P., 2011, ApJ, 727, 73

Ciardi B., Bolton J. S., Maselli A., Graziani L., 2012, MNRAS, 423, 558

Covino S. et al., 2013, MNRAS, 432, 1231

Cucchiara A. et al., 2011a, ApJ, 736, 7

Cucchiara A. et al., 2011b, ApJ, 743, 154

Cucchiara A., 2010, GCN Circ., No. 10478

Cucchiara A., Fox D. B., Cenko S. B., Berger E., 2008a, GCN Circ., No. 10478

Cucchiara A., Fox D. B., Cenko S. B., Berger E., 2008b, GCN Circ., No. 8713

Cucchiara A., Cenko S. B., Perley D. A., 2014, GCN Circ., No. 16856

Cucchiara A., Fumagalli M., Rafelski M., Kocevski D., Prochaska J. X., Cooke R. J., Becker G. D., 2015, ApJ, 804, 51

D'Avanzo P. et al., 2010, A&A, 522, A20

D'Avanzo P., Malesani D., D'Elia V., Antonelli L. A., Tagliaferri G., Vergani S. D., Fiorenzano A., Mainella G., 2014, GCN Circ., No. 16493

D'Avanzo P., Malesani D., D'Elia V., Melandri A., Lorenzi V., Stoev H., 2016, GCN Circ., No. 20078

D'Elia V., Thoene C. C., de Ugarte Postigo A., D'Avanzo P., Covino S., Piranomonte S., Salvaterra R., Chincarini G., 2008, GCN Circ., No. 8531

D'Elia V., D'Avanzo P., Covino S., Melandri A., Vergani S. D., di Fabrizio L., 2014, GCN Circ., No. 15802

de Barros S. et al., 2016, A&A, 585, A51

De Cia A. et al., 2011, MNRAS, 418, 129

de Ugarte Postigo A. et al., 2012, A&A, 548, A11

de Ugarte Postigo A., Tomasella L., 2015, GCN Circ., No. 17710

de Ugarte Postigo A., Thoene C. C., Gorosabel J., Sanchez-Ramirez R., Fynbo J. P. U., Tanvir N. R., Cabrera-Lavers A., Garcia A., 2013, GCN Circ., No. 15470

de Ugarte Postigo A., Blazek M., Janout P., Sprimont P., Thöne C. C., Gorosabel J., Sánchez-Ramírez R., 2014a, Proc SPIE, Software and Cyberinfrastructure for Astronomy III. SPIE, Bellingham, p. 91520B

de Ugarte Postigo A., Thöne C. C., Tanvir N. R., Gorosabel J., Fynbo J., Lombardi G., Reverte-Paya D., Perez D., 2014b, GCN Circ., No. 16968

de Ugarte Postigo A., Tanvir N. R., Cano Z., Izzo L., Fynbo J. P. U., Sanchez-Ramirez R., Thoene C. C., Pesev P., 2016, GCN Circ., No. 19245

de Ugarte Postigo A., Kann D. A., Thoene C., Izzo L., Tanvir N. R., Lombardi G., Marante A., 2017a, GCN Circ., No. 20990

de Ugarte Postigo A., Izzo L., Kann D. A., Thoene C., Cano Z., Fynbo J. P. U., Garcia Alvarez D., 2017b, GCN Circ., No. 21177

de Ugarte Postigo A., Cano Z., Izzo L., Thoene C. C., Kann D. A., Castro-Rodriguez N., Valladares D. P., 2018, GCN Circ., No. 22346

Detmers R. G., Langer N., Podsiadlowski P., Izzard R. G., 2008, A&A, 484, 831

Doran E. I. et al., 2013, A&A, 558, A134

Dove J. B., Shull J. M., Ferrara A., 2000, ApJ, 531, 846

Eldridge J. J., Stanway E. R., 2009, MNRAS, 400, 1019

Evans P. A. et al., 2009, MNRAS, 397, 1177

Faisst A. L., 2016, ApJ, 829, 99

Fatkhullin T. et al., 2009, GCN Circ., No. 9712

Faucher-Giguère C.-A., Lidz A., Zaldarriaga M., Hernquist L., 2009, ApJ, 703, 1416

Ferrero P. et al., 2009, A&A, 497, 729

Finkelstein S. L. et al., 2012, ApJ, 758, 93

Fiore F. et al., 2005, ApJ, 624, 853

Fontanot F., Cristiani S., Pfrommer C., Cupani G., Vanzella E., 2014, MNRAS, 438, 2097

Fox A. J., Ledoux C., Vreeswijk P. M., Smette A., Jaunsen A. O., 2008, A&A, 491, 189

Fragos T., Lehmer B. D., Naoz S., Zezas A., Basu-Zych A., 2013, ApJ, 776, L31

Friis M. et al., 2015, MNRAS, 451, 167

Fruchter A. S. et al., 2006, Nature, 441, 463

Fynbo J. P. U. et al., 2002, in Gilfanov M., Sunyeav R., Churazov E., eds, Lighthouses of the Universe: The Most Luminous Celestial Objects and Their Use for Cosmology. Springer, Berlin, p. 187

Fynbo J. P. U. et al., 2005, ApJ, 633, 317

Fynbo J. P. U. et al., 2009, ApJS, 185, 526

Fynbo J. P. U., de Ugarte Postigo A., D'Elia V., Tanvir N. R., Pugliese G., Kann D. A., Malesani D. B., Heintz K. E., 2018, GCN Circ., No. 23356

Gehrels N., Razzaque S., 2013, Frontiers Phys., 8, 661

Gnedin N. Y., Kravtsov A. V., Chen H.-W., 2008, ApJ, 672, 765

Gorosabel J., de Ugarte Postigo A., Thöne C., Perley D., Garcia Rodriguez A., 2014, GCN Circ., No. 16671

Götberg Y., de Mink S. E., Groh J. H., 2017, A&A, 608, A11

Graham J. F., Fruchter A. S., 2017, ApJ, 834, 170

Granot J., Sari R., 2002, ApJ, 568, 820

Grazian A. et al., 2017, A&A, 602, A18

Greiner J. et al., 2009a, ApJ, 693, 1610

Greiner J. et al., 2009b, ApJ, 693, 1912

Greiner J. et al., 2011, A&A, 526, A30

Greiner J. et al., 2015a, Nature, 523, 189

Greiner J. et al., 2015b, ApJ, 809, 76

Gunn J. E., Peterson B. A., 1965, ApJ, 142, 1633

Hansen S. H., Haiman Z., 2004, ApJ, 600, 26

Hascoët R., Uhm Z. L., Mochkovitch R., Daigne F., 2011, A&A, 534, A104

Hassan S., Davé R., Mitra S., Finlator K., Ciardi B., Santos M. G., 2018, MNRAS, 473, 227

Heintz K. E. et al., 2018, MNRAS, 479, 3456

Hjorth J. et al., 2003a, Nature, 423, 847

Hjorth J. et al., 2003b, ApJ, 597, 699

Hjorth J., Bloom J. S., 2012, in Kouveliotou C., Wijers R. A. M. J., Woosley S., eds, Chapter 9 in 'Gamma-Ray Bursts", Cambridge Astrophysics Series 51. Cambridge University Press, Cambridge, p. 169

Howard C. S., Pudritz R. E., Harris W. E., Klessen R. S., 2018, MNRAS, 475, 3121

Hunt L. K. et al., 2014, A&A, 565, A112

Izzo L. et al., 2018, GCN Circ., No. 22567

Jakobsson P. et al., 2004, A&A, 427, 785

Jakobsson P. et al., 2006, A&A, 460, L13

Jakobsson P. et al., 2012, ApJ, 752, 62

Japelj J. et al., 2016, A&A, 590, A129

Japelj J. et al., 2017, MNRAS, 468, 389

Jensen B. L. et al., 2001, A&A, 370, 909

Jeong S., Sanchez-Ramirez R., Gorosabel J., Castro-Tirado A. J., 2014, GCN Circ., No. 15936

Kann D. A. et al., 2010, ApJ, 720, 1513

Kann D. A. et al., 2018, A&A, 617, A122

Kelly P. L., Kirshner R. P., Pahre M., 2008, ApJ, 687, 1201

Kelly P. L., Filippenko A. V., Modjaz M., Kocevski D., 2014, ApJ, 789, 23

Khaire V., Srianand R., Choudhury T. R., Gaikwad P., 2016, MNRAS, 457, 4051

Kimm T., Cen R., 2014, ApJ, 788, 121

Kistler M. D., Yüksel H., Beacom J. F., Hopkins A. M., Wyithe J. S. B., 2009, ApJ, 705, L104

Knevitt G., Wynn G. A., Power C., Bolton J. S., 2014, MNRAS, 445, 2034

Krongold Y., Prochaska J. X., 2013, ApJ, 774, 115

Krühler T. et al., 2015, A&A, 581, A125

Kuhlen M., Faucher-Giguère C.-A., 2012, MNRAS, 423, 862

Kuin N. P. M. et al., 2009, MNRAS, 395, L21

Larsson J., Levan A. J., Davies M. B., Fruchter A. S., 2007, MNRAS, 376, 1285

Laskar T. et al., 2014, ApJ, 781, 1

Laskar T., Berger E., Chary R.-R., 2011, ApJ, 739, 1

Levan A. J. et al., 2014, ApJ, 781, 13

Levesque E. M. et al., 2010a, MNRAS, 401, 963

Levesque E. M., Soderberg A. M., Kewley L. J., Berger E., 2010b, ApJ, 725, 1337

Lockman F. J., Jahoda K., McCammon D., 1986, ApJ, 302, 432

Lyman J. D. et al., 2017, MNRAS, 467, 1795

Ma X., Hopkins P. F., Kasen D., Quataert E., Faucher-Giguère C.-A., Kereš D., Murray N., Strom A., 2016, MNRAS, 459, 3614

Madau P., Dickinson M., 2014, ARA&A, 52, 415

Madau P., Fragos T., 2017, ApJ, 840, 39

Madau P., Haardt F., 2015, ApJ, 813, L8

Malesani D. et al., 2014, GCN Circ., No. 15800

Malesani D., Fynbo J. P. U., D'Elia V., de Ugarte Postigo A., Jakobsson P., Thoene C. C., 2009, GCN Circ., No. 9457

Marchi F. et al., 2017, A&A, 601, A73

McGuire J. T. W. et al., 2016, ApJ, 825, 135

Melandri A. et al., 2008, ApJ, 686, 1209

Melandri A. et al., 2015, A&A, 581, A86

Mirabal N., Melandri A., Halpern J. P., 2007, GCN Circ., No. 6162

Mirabel I. F., Dijkstra M., Laurent P., Loeb A., Pritchard J. R., 2011, A&A, 528, A149

Molinari E. et al., 2007, A&A, 469, L13

Morgan A. N. et al., 2014, MNRAS, 440, 1810

Mostardi R. E., Shapley A. E., Nestor D. B., Steidel C. C., Reddy N. A., Trainor R. F., 2013, ApJ, 779, 65

Møller P. et al., 2002, A&A, 396, L21

Nestor D. B., Shapley A. E., Kornei K. A., Steidel C. C., Siana B., 2013, ApJ, 765, 47

Nicuesa Guelbenzu A. et al., 2011, A&A, 531, L6

Nysewander M., Reichart D. E., Crain J. A., Foster A., Haislip J., Ivarsen K., Lacluyze A., Trotter A., 2009, ApJ, 693, 1417

Ochsendorf B. B., Meixner M., Roman-Duval J., Rahman M., Evans N. J., II, 2017, ApJ, 841, 109

Oey M. S., Clarke C. J., 1997, MNRAS, 289, 570

Ouchi M. et al., 2009, ApJ, 706, 1136

Page K. L. et al., 2009, MNRAS, 400, 134

Patel M., Warren S. J., Mortlock D. J., Fynbo J. P. U., 2010, A&A, 512, L3

Pellegrini E. W., Oey M. S., Winkler P. F., Points S. D., Smith R. C., Jaskot A. E., Zastrow J., 2012, ApJ, 755, 40

Perley D. A. et al., 2008, ApJ, 688, 470

Perley D. A. et al., 2010, MNRAS, 406, 2473

Perley D. A. et al., 2013, ApJ, 778, 128

Perley D. A. et al., 2015, ApJ, 801, 102

Perley D. A. et al., 2016a, ApJ, 817, 7

Perley D. A. et al., 2016b, ApJ, 817, 8

Perley D. A., 2011, PhD thesis. Univ. California

Perley D. A., 2014, GCN Circ., No. 16181

Perna R., Lazzati D., 2002, ApJ, 580, 261

Planck Collaboration XIII 2016, A&A, 596, A108

Podsiadlowski P., Ivanova N., Justham S., Rappaport S., 2010, MNRAS, 406, 840

Pontzen A. et al., 2010, MNRAS, 402, 1523

Prochaska J. X., Chen H.-W., Bloom J. S., 2006, ApJ, 648, 95

Prochaska J. X., Chen H.-W., Dessauges-Zavadsky M., Bloom J. S., 2007, ApJ, 666, 267

Prochaska J. X., Perley D., Howard A., Chen H.-W., Marcy G., Fischer D., Wilburn C., 2008, GCN Circ., No. 8083

Rahner D., Pellegrini E. W., Glover S. C. O., Klessen R. S., 2017, MNRAS, 470, 4453

Razoumov A. O., Sommer-Larsen J., 2010, ApJ, 710, 1239

Robertson B. E., Ellis R. S., 2012, ApJ, 744, 95

Robertson B. E., Ellis R. S., Furlanetto S. R., Dunlop J. S., 2015, ApJ, 802, L19

Rol E. et al., 2007, GCN Circ., No. 6221

Rossi A. et al., 2012, A&A, 545, A77

Rossi A., Gargiulo A., Malesani D. B., Vergani S. D., D'Elia V., Campana S., 2018, GCN Circ., No. 22845

Roy A., Nath B. B., Sharma P., 2015, MNRAS, 451, 1939

Rutkowski M. J. et al., 2017, ApJ, 841, L27

Sabbi E. et al., 2016, ApJS, 222, 11

Safarzadeh M., Scannapieco E., 2016, ApJ, 832, L9

Salvaterra R. et al., 2009, Nature, 461, 1258

Sana H. et al., 2012, Science, 337, 444

Sánchez-Ramírez R. et al., 2013a, Rev. Mex. Astron. Astrofis. Ser. Conf., 42, 113

Sanchez-Ramirez R., Gorosabel J., Castro-Tirado A. J., Cepa J., Gomez-Velarde G., 2013b, GCN Circ., No. 14685

Savaglio S. et al., 2012, MNRAS, 420, 627

Schady P., Savaglio S., Krühler T., Greiner J., Rau A., 2011, A&A, 525, A113

Schaerer D., Boone F., Zamojski M., Staguhn J., Dessauges-Zavadsky M., Finkelstein S., Combes F., 2015, A&A, 574, A19

Schlafly E. F., Finkbeiner D. P., 2011, ApJ, 737, 103

Schulze S. et al., 2015, ApJ, 808, 73

Sciama D. W., 1982, MNRAS, 198, 1P

Selsing J. et al., 2018, preprint(arXiv:1802.07727)

Shapley A. E., Steidel C. C., Pettini M., Adelberger K. L., Erb D. K., 2006, ApJ, 651, 688

Shapley A. E., Steidel C. C., Strom A. L., Bogosavljević M., Reddy N. A., Siana B., Mostardi R. E., Rudie G. C., 2016, ApJ, 826, L24

Sharma M., Theuns T., Frenk C., Bower R., Crain R., Schaller M., Schaye J., 2016, MNRAS, 458, L94

Shin M.-S. et al., 2006, preprint(arXiv:astro-ph/0608327)

Siana B. et al., 2015, ApJ, 804, 17

Smette A., Ledoux C., Vreeswijk P., De Cia A., Petitjean P., Fynbo J., Malesani D., Fox A., 2013, GCN Circ., No. 14848

Stanway E. R., Eldridge J. J., Becker G. D., 2016, MNRAS, 456, 485

Starling R. L. C., Wijers R. A. M. J., Hughes M. A., Tanvir N. R., Vreeswijk P. M., Rol E., Salamanca I., 2005, MNRAS, 360, 305

Steidel C. C., Pettini M., Adelberger K. L., 2001, ApJ, 546, 665

Steidel C. C., Bogosavlevic M., Shapley A. E., Reddy N. A., Rudie G. C., Pettini M., Trainor R. F., Strom A. L., 2018 ApJ, 869, 123

Svensson K. M., Levan A. J., Tanvir N. R., Fruchter A. S., Strolger L.-G., 2010, MNRAS, 405, 57

Tanvir N. R. et al., 2009, Nature, 461, 1254

Tanvir N. R. et al., 2012a, ApJ, 754, 46

Tanvir N. R. et al., 2018, ApJ, 865, 107

Tanvir N. R., Wiersema K., Levan A. J., Cenko S. B., Geballe T., 2011, GCN Circ., No. 12225

Tanvir N. R., Levan A. J., Matulonis T., 2012b, GCN Circ., No. 14009

Tetzlaff N., Neuhäuser R., Hohle M. M., 2011, MNRAS, 410, 190

Thoene C. C. et al., 2009, GCN Circ., No. 9409

Thöne C. C. et al., 2011, MNRAS, 414, 479

Thöne C. C., Perley D. A., Cooke J., Bloom J. S., Chen H.-W., Barton E., 2007, GCN Circ., No. 6741

Thöne C. C., de Ugarte Postigo A., Gorosabel J., Sanchez-Ramirez R., Fynbo J. P. U., Gomez Velarde G., 2012, GCN Circ., No. 13628

Torii K., 2005, GCN Circ., No. 3943

Totani T., Kawai N., Kosugi G., Aoki K., Yamada T., Iye M., Ohta K., Hattori T., 2006, PASJ, 58, 485

Toy V. L. et al., 2016, ApJ, 832, 175

Trebitsch M., Blaizot J., Rosdahl J., Devriendt J., Slyz A., 2017, MNRAS, 470, 224

Trenti M., Perna R., Jimenez R., 2015, ApJ, 802, 103

Updike A. C. et al., 2008, ApJ, 685, 361

van den Heuvel E. P. J., Portegies Zwart S. F., 2013, ApJ, 779, 114

van Marle A. J., Langer N., Achterberg A., García-Segura G., 2006, A&A, 460, 105

van Marle A. J., Langer N., Yoon S.-C., García-Segura G., 2008, A&A, 478, 769

Vanzella E. et al., 2010, ApJ, 725, 1011

Vanzella E. et al., 2012, ApJ, 751, 70

Vanzella E. et al., 2015, A&A, 576, A116

Vanzella E. et al., 2016, ApJ, 825, 41

Varela K., Kann D. A., Klose S., Greiner J., 2014, GCN Circ., No. 16849

Vergani S. D. et al., 2017, A&A, 599, A120

Vreeswijk P. M. et al., 2004, A&A, 419, 927

Vreeswijk P. M. et al., 2006, A&A, 447, 145

Vreeswijk P. M. et al., 2007, A&A, 468, 83

Vreeswijk P. M. et al., 2013, A&A, 549, A22

Vreeswijk P. M., Fynbo J. P. U., Malesani D., Hjorth J., de Ugarte Postigo A., 2008, GCN Circ., No. 8191

Walch S. K., Whitworth A. P., Bisbas T., Wünsch R., Hubber D., 2012, MNRAS, 427, 625

Watson D. et al., 2013, ApJ, 768, 23

Watson D., Jakobsson P., 2012, ApJ, 754, 89

Watson D., Hjorth J., Fynbo J. P. U., Jakobsson P., Foley S., Sollerman J., Wijers R. A. M. J., 2007, ApJ, 660, L101

Waxman E., Draine B. T., 2000, ApJ, 537, 796

Wiersema K., Levan A., Kamble A., Tanvir N., Malesani D., 2009, GCN Circ., No. 9673

Willingale R., Starling R. L. C., Beardmore A. P., Tanvir N. R., O'Brien P. T., 2013, MNRAS, 431, 394

Wiseman P., Perley D. A., Schady P., Prochaska J. X., de Ugarte Postigo A., Krühler T., Yates R. M., Greiner J., 2017, A&A, 607, A107

Wise J. H., Demchenko V. G., Halicek M. T., Norman M. L., Turk M. J., Abel T., Smith B. D., 2014, MNRAS, 442, 2560

Xu D. et al., 2013, ApJ, 776, 98

Xu D., Tanvir N. R., Malesani D., Fynbo J. P. U., Jakobsson P., Saario J., 2015, GCN Circ., No. 18696

Xu H., Wise J. H., Norman M. L., Ahn K., O'Shea B. W., 2016a, ApJ, 833, 84

Xu D., Fynbo J. P. U., Malesani D., de Ugarte Postigo A., Petrushevska T., Saario J., Telting J., 2016b, GCN Circ., No. 19109

Yoon S.-C., Langer N., 2005, A&A, 443, 643

Yoon S.-C., Langer N., Norman C., 2006, A&A, 460, 199

Yuan W. et al., 2016, Space Sci. Rev., 202, 235

Zackrisson E., Inoue A. K., Jensen H., 2013, ApJ, 777, 39

Zafar T. et al., 2018a, MNRAS, 480, 108

Zafar T., 2018b, ApJ, 860, L21

Zafar T., Watson D. J., Tanvir N. R., Fynbo J. P. U., Starling R. L. C., Levan A. J., 2011, ApJ, 735, 2

APPENDIX A: INDIVIDUAL BURSTS

In this appendix we provide information about selected GRBs. In particular, we present our Ly α fits for those cases where the column densities have not previously been reported and are not included in Selsing et al. (2018). Unless stated otherwise, the precise redshift is taken from metal absorption lines seen in the spectra, which reduces the free parameters, and improves accuracy of the fits. Details of the fitting procedure are given in Selsing et al. (2018), which employs a visual estimate of the best fit and range of plausible models. This approach allows easy accounting for anomalies in the data and is more consistent with the historical results that form a large part of our sample. A comparison of a sub-set of spectra using a more formal fitting procedure shows excellent agreement in the derived H I column densities, and that our error bars are generally conservative (Bolmer et al. 2018a).

We caution that the nature of target-of-opportunity observations of variable sources means that the source magnitude is frequently poorly known prior to observation; in many cases, there was limited time available and non-optimal conditions or sky location. Thus, some of the spectra are unusually low signal-to-noise and/or suffer from imperfect flux calibration or other anomalies. Furthermore, there are cases where host galaxy emission, including Ly α emission lines, contaminates the afterglow signal, and where intervening absorbers introduce metal lines. However, fortunately for the purposes of this analysis, the red-wing of the Ly α absorption features can still be measured to an adequate level of precision, with little overall systematic bias in determination of $N_{\rm HI}$.

Data are taken from various sources: some from observations we obtained ourselves and in other cases from archives. Spectrographs used include the Gemini Multi-Object Spectrograph North and South (GMOS-N, GMOS-S), the VLT FOcal Reducer and low dispersion Spectrograph (FORS1 and FORS2) and UltraViolet Echelle Spectrograph (UVES), the William Herschel Telescope (WHT) Intermediate dispersion Spectrograph and Imaging System (ISIS) and Auxiliary port CAMera (ACAM), the Gran Telescopio Canarias (GTC) Optical System for Imaging and low-Intermediate-Resolution Integrated Spectroscopy (OSIRIS), the Nordic Optical Telescope (NOT) Andalucia Faint Object Spectrograph and Camera (ALFOSC), the Telescopio Nazionale Galileo (TNG) Device Optimized for the Low Resolution (DOLoRes), the Asiago Copernico Telescope (CT) Asiago Faint Object Spectrograph and Camera (AFOSC), the Keck Low Resolution Imaging Spectrograph (LRIS), and the Large Binocular Telescope (LBT) Multi-Object Double Spectrograph (MODS).

Spectra presented in this appendix will be made available in the GRBspec data base http://grbspec.iaa.es (de Ugarte Postigo et al. 2014a).

A1 GRB 021004

The bright afterglow of GRB 021004 was well studied, and spectroscopy revealed an unusually complex velocity structure for the absorbing gas (Fiore et al. 2005; Starling et al. 2005; Castro-Tirado et al. 2010). Combined with saturation of the lines, establishing the H I column density was not straight-forward, and here we adopt a reasonable value and error based on the $\log(N_{\rm HI}/{\rm cm}^{-2}) > 18$ from the absence of continuum below the Lyman limit (Fynbo et al. 2005)

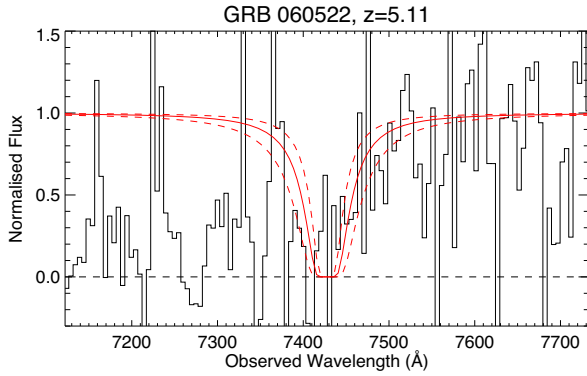**Figure A1.** Fit of the red wing of Ly α for the GRB 060522 Keck-I/LRIS spectrum.

Figure A2. Fit of the red wing of Ly α for the GRB 070810A Keck-I/LRIS spectrum.

and $\log(N_{\rm HI}/{\rm cm}^{-2}) < 20$ from analysis of the multiple Ly α lines themselves (Møller et al. 2002).

A2 GRB 060522

GRB 060522 was observed with Keck-I/LRIS, starting 14:24 UT on 2006 May 22. A total exposure of 1800 s was obtained. The fit to the Ly α line is shown in Fig. A1; the inferred column $\log(N_{\rm HI}/{\rm cm}^{-2}) = 20.6 \pm 0.3$ is consistent with previous estimates (Cenko et al. 2006; Chary et al. 2007). Note, the region redwards of Ly α is badly affected by fringing, impeding searches for metal absorption lines.

A3 GRB 070223

Near-IR imaging of GRB 070223 was obtained with the WHT Long-slit Intermediate Resolution Infrared Spectrograph (LIRIS) instrument in the *JHK* filters between 2.7 and 3.7 h post-burst. A faint source was detected at the location of the X-ray afterglow (Rol et al. 2007), for which we find a magnitude $K_{\rm AB} = 21.9 \pm 0.3$ calibrated against 2MASS stars in the field (and corrected for small foreground extinction via Schlafly & Finkbeiner 2011). Subsequent imaging obtained 8 d post-burst showed this source to have declined to $K_{\rm AB} = 22.8 \pm 0.2$ mag, confirming the identification of the afterglow, but also indicating the presence of an underlying host galaxy (also detected in 3.6 μm *Spitzer* imaging by Perley et al. 2016b).

GRB 070223 was observed rapidly with the 2 m Liverpool Telescope (LT) in various optical filters, beginning only 18 min postburst (Melandri et al. 2008). We created a 30 min stacked integration from *r*-band imaging taken between 3 and 3.7 h post-burst. At the location of the *K*-band transient, there is a faint detection of a source with foreground corrected magnitude $r = 23.8 \pm 0.3$, calibrated against SDSS stars in the field. This object was also seen in *R*-band early imaging by the MDM 1.3 m telescope (Rol et al. 2007), but, as detailed in the text, appears to be a constant source, presumably the host galaxy.

A4 GRB 070810A

GRB 070810A was observed with Keck-I/LRIS, starting 05:47 UT on 2007 August 10. A total exposure of 2 × 600 s was obtained (Thöne et al. 2007). The fit to the Ly α line is shown in Fig. A2.
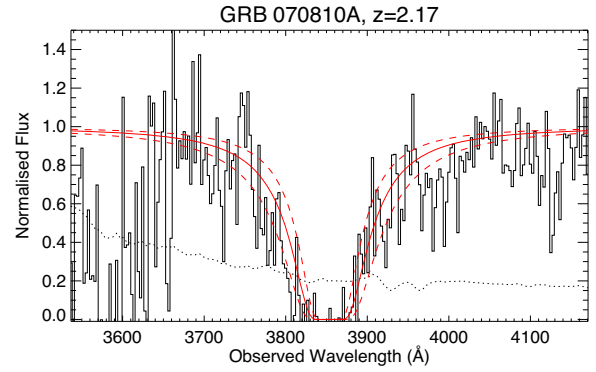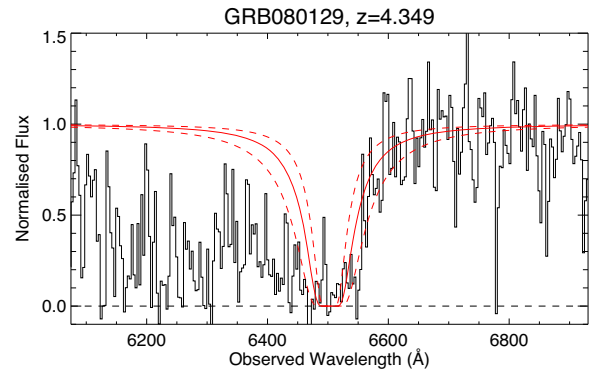
Figure A3. Fit of the red wing of Ly α for the GRB 080129 VLT/FORS1 spectrum.

A5 GRB 080129

GRB 080129 was observed with VLT/FORS1, starting 05:24 UT on 2008 January 30. A total exposure of 4 × 1800 s was obtained with the OG590 blocking filter and 300I grism, and reduced with the standard ESO pipeline (Greiner et al. 2009b). The redshift is fixed to that of the metal absorption lines, and the fit to the red wing of Ly α (Fig. A3) is rather poor in this case, plausibly due to velocity structure in low metallicity and low column-density gas close to the host.

A6 GRB 080810

GRB 080810 was observed at high resolution by Keck/HIRES (Prochaska et al. 2008), and the spectrum showed a somewhat complex H I absorption system, with two main components separated by $\approx 700\,{\rm km\,s}^{-1}$. The lower redshift system showed Si II* fine-structure lines, suggesting this gas was closer to the GRB location, and likely that the other system is infalling on the near-side. Page et al. (2009) found an upper limit for the combined absorber of $\log(N_{\rm HI}/{\rm cm}^{-2}) < 19.5$ and a lower limit for the higher redshift component of $\log(N_{\rm HI}/{\rm cm}^{-2}) > 17.7$ from the absence of emission below the Lyman limit. Recently, Wiseman et al. (2017) reanalysed the HIRES spectrum, finding $\log(N_{\rm HI}/{\rm cm}^{-2}) = 18.10 \pm 0.25$ for this dominant component, which we use here.
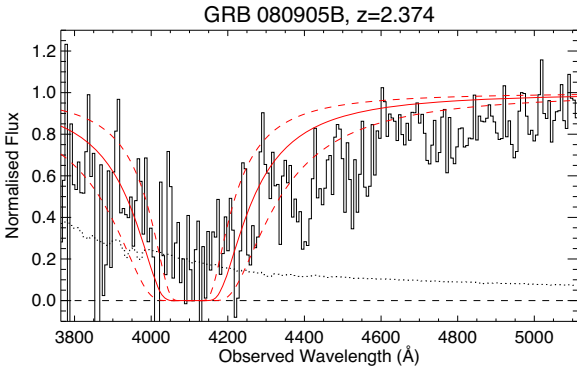
Figure A4. Fit of the red wing of Ly α for the GRB 080905B VLT/FORS2 spectrum.

A7 GRB 080905B

GRB 080905B was observed by VLT/FORS2, starting 01:16 UT on 2008 September 6. A total exposure of $2 \times 600\,\mathrm{s}$ was obtained with the GRIS_300V grism, and reduced with the standard ESO pipeline (Vreeswijk et al. 2008). The fit to the Ly α line is shown in Fig. A4.

A8 GRB 080913

GRB 080913 was observed with VLT/FORS2, being found to be at redshift $z \approx 6.7$ from the location of the Ly α break by Greiner et al. (2009a). Lacking a precise metal line redshift, Greiner et al. (2009a) were only able to place weak constraints on the H I column density concluding $20.3 < \log(N_{\mathrm{HI}}/\mathrm{cm}^{-2}) < 21.4$. A subsequent reanalysis of the spectrum by Patel et al. (2010) located a weak S II + Si II blend, establishing a firmer redshift of $z = 6.733$. This allowed a more precise determination of the H I column density, $\log(N_{\mathrm{HI}}/\mathrm{cm}^{-2}) = 19.84$ assuming no neutral component of the IGM, and $\log(N_{\mathrm{HI}}/\mathrm{cm}^{-2}) = 19.6$ in a fit that allowed the neutral fraction of the IGM to be a free parameter (specifically they found $x_{H\,I} = 0.06$). Given this uncertainty, and the poor S/N of the spectrum, we adopt $\log(N_{\mathrm{HI}}/\mathrm{cm}^{-2}) = 19.6 \pm 0.3$ here.

A9 GRB 081029

GRB 081029 was observed by Gemini/GMOS-S, starting 07:04 UT on 2008 October 29 (Cucchiara et al. 2008a). A total exposure of $2 \times 900\,\mathrm{s}$ was obtained with the R400 grating set at 6000 Å central wavelength and reduced using the standard Gemini reduction tools within IRAF. The fit to the Ly α line is shown in Fig. A5. Although there is a hint of Ly α emission in the trough, it does not affect the quality of the fit.

A10 GRB 081118

GRB 081118 was observed by VLT/FORS2, starting 02:48 UT on 2008 November 19. A total exposure of $2 \times 1800\,\mathrm{s}$ was obtained with the GRIS_300V grism, and reduced with the standard ESO pipeline (D'Elia et al. 2008). The fit to the Ly α line is shown in Fig. A6.

A11 GRB 081222

GRB 081222 was observed by Gemini/GMOS-S, starting 01:02 UT on 2008 December 23 (Cucchiara et al. 2008b). A total exposure of $2 \times 900\,\mathrm{s}$ was obtained with the R400 grating set at 6000 Å central
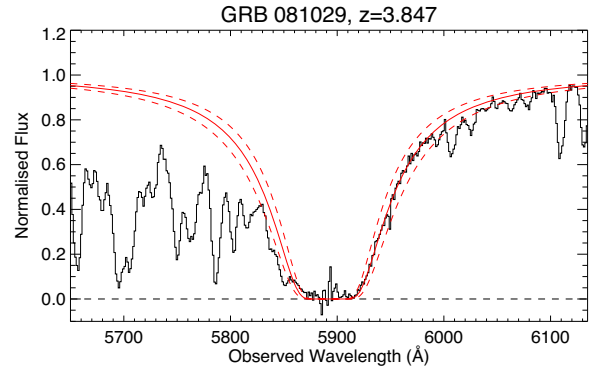
Figure A5. Fit of the red wing of Ly α for the GRB 081029 Gemini/GMOS-S spectrum.
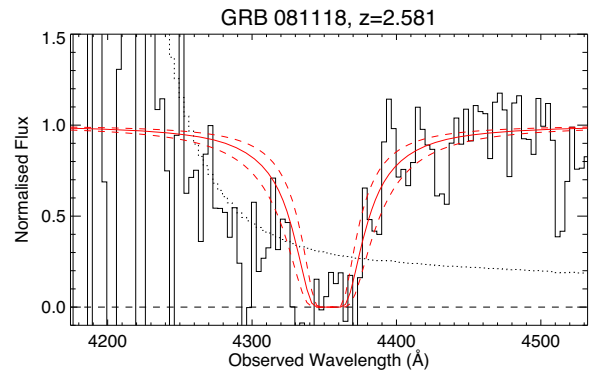
Figure A6. Fit of the red wing of Ly α for the GRB 081118 VLT/FORS2 spectrum.
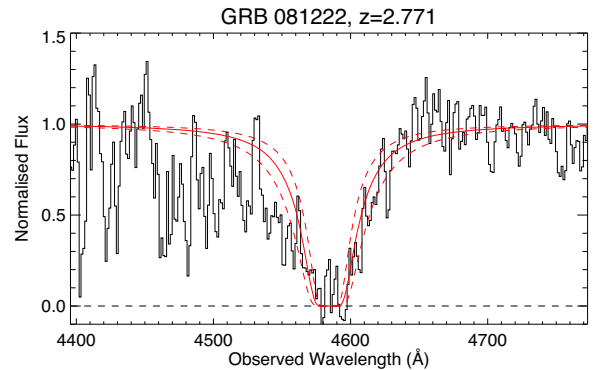
Figure A7. Fit of the red wing of Ly α for the GRB 081222 Gemini/GMOS-S spectrum.

wavelength, and reduced using the standard Gemini reduction tools within IRAF. The fit to the Ly α line is shown in Fig. A7.

A12 GRB 090313

GRB 090313 was observed by Gemini/GMOS-S, starting 04:20 UT on 2009 March 14 (Chornock et al. 2009a). A total exposure of $2 \times 600\,\mathrm{s}$ was obtained with the R400 grating set at 6000 Å central wavelength, and reduced using the standard Gemini reduction tools within IRAF. The fit to the Ly α line is shown in Fig. A8.
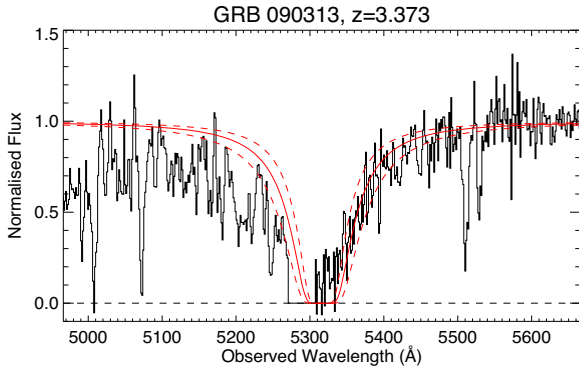
Figure A8. Fit of the red wing of Ly α for the GRB 090313 Gemini/GMOS-S spectrum. Note that there is a gap between chips of the camera around 5280 Å. This produces an anomaly in the trace that was ignored in the fit.

A13 GRB 090323

GRB 090323 was unusual exhibiting two absorption systems separated by $\approx 700\,\mathrm{km\,s^{-1}}$, and a relatively high metal abundance (Savaglio et al. 2012). In this case both systems showed Si II∗ fine structure lines, likely indicating fairly close proximity to the GRB. The value for N_{HI} used here was obtained by summing the column densities of the two systems.

A14 GRB 090426

The prompt duration of GRB 090426 was $T_{90} \approx 1.3$ s, suggesting it could be a short-duration burst, particularly given that cosmological time-dilation makes this less than 0.4 s in the source-frame. However, since it was intrinsically bright and took place in an interacting star-forming system (Thöne et al. 2011), we include it in our sample as a possible long-duration GRB (see also Nicuesa Guelbenzu et al. 2011). The H I column density in this case was seen to vary, and we take here that measured at 1.1 h post-burst by Levesque et al. (2010a) using Keck/LRIS. Removing GRB 090426 from the sample would not have a significant effect on any of the conclusions.

A15 GRB 090519

GRB 090519 was observed by VLT/FORS2 starting at 01:03 UT on 2009 May 20 (Thoene et al. 2009). A total exposure of 3×1800 s was obtained, covering the wavelength range 3500–9200 Å. The fit to the Ly α line is shown in Fig. A9. The afterglow was faint, and the redshift is estimated from the Ly α and Ly β breaks since no clear metal lines were seen.

A16 GRB 090529

GRB 090529 was observed by VLT/FORS2 starting at 01:52 UT on 2009 May 31, roughly 1.5 d post-burst (Malesani et al. 2009). A total exposure of 2×1800 s was obtained, covering the wavelength range 3500–9200 Å. The fit to the Ly α line is shown in Fig. A10. Although the S/N is unusually poor (largely due to the lateness of the observation), the fit benefits from the redshift being fixed by metal absorption lines.

A17 GRB 090715B

GRB 090715B was observed with the WHT/ISIS starting 23:46 UT on 2009 July 15 (Wiersema et al. 2009). This spectrograph has a
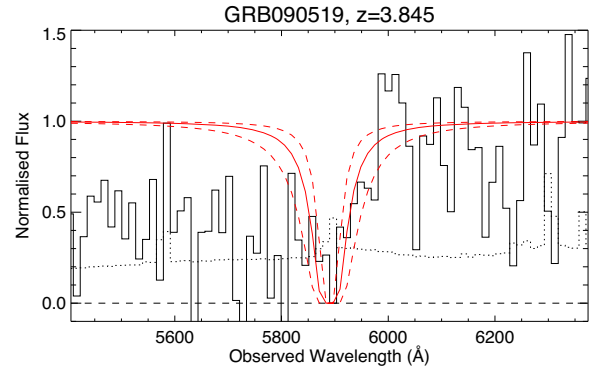
Figure A9. Fit of the red wing of Ly α for the GRB 090519 VLT/FORS2 spectrum.
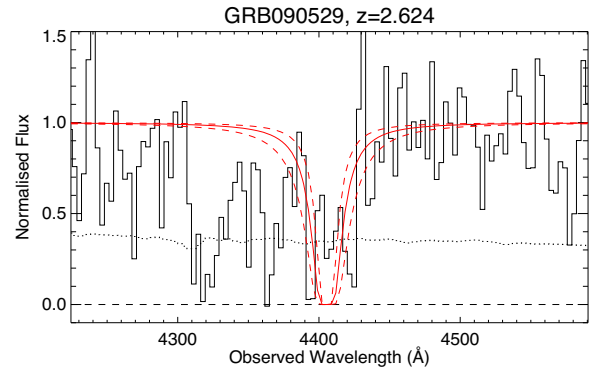
Figure A10. Fit of the red wing of Ly α for the GRB 090529 VLT/FORS2 spectrum.
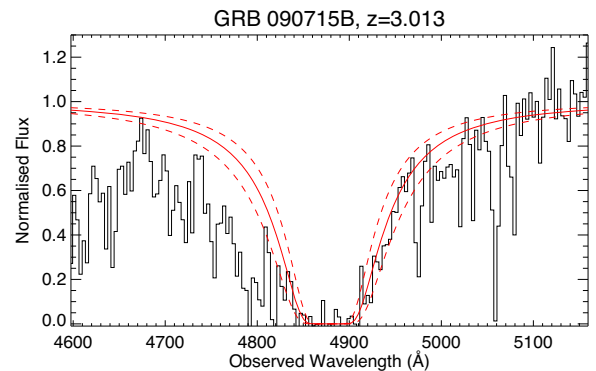
Figure A11. Fit of the red wing of Ly α for the GRB 090715B WHT/ISIS spectrum.

blue and a red arm, separated by a dichroic; we used the 300B and 316R gratings. Spectroscopic observations consisted of 4×900 s exposure time. The data were reduced using standard techniques in IRAF. Several metal absorption lines give a redshift $z = 3.01$. The fit to the Ly α line is shown in Fig. A11.

A18 GRB 090726

GRB 090726 was observed by the SAO RAS 6-m telescope using the SCORPIO spectrograph starting at 00:15 UT on 2009 July 27 (Fatkhullin et al. 2009). A total exposure of 600 s was obtained,
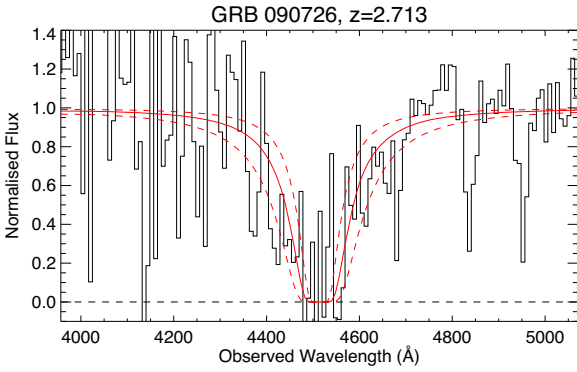
Figure A12. Fit of the red wing of Ly α for the GRB 090726 SAO RAS 6-m / SCORPIO spectrum.
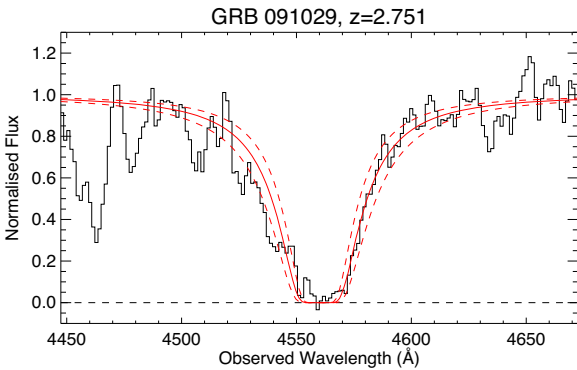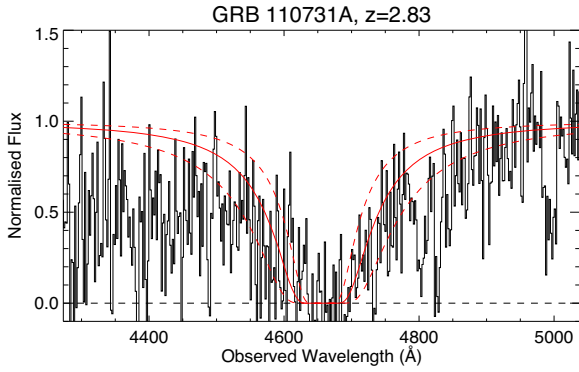

Figure A13. Fit of the red wing of Ly α for the GRB 091029 Gemini/GMOS-S spectrum.

covering the wavelength range 3700–7800 Å. The fit to the Ly α line is shown in Fig. A12.

A19 GRB 091029

GRB 091029 was observed by Gemini/GMOS-S, starting 06:05 UT on 2009 October 29 (Chornock, Perley & Cobb 2009b). A total exposure of 4 × 600 s was obtained with the R400 grating set at 6000 Å central wavelength and reduced using the standard Gemini reduction tools within IRAF. The fit to the Ly α line is shown in Fig. A13.

A20 GRB 100302A

GRB 100302A was observed by Gemini/GMOS-N, starting 09:42 UT on 2010 March 3 (Chornock et al. 2010). A total exposure of 1200 s was obtained with the R400 grating. The continuum S/N is rather poor, but weak metal lines indicate a redshift of $z = 4.813$. The fit to the Ly α red wing is shown in Fig. A14.

A21 GRB 100316A

GRB 100316A was observed by GTC/OSIRIS, starting 06:13 UT on 2010 March 16 (Sánchez-Ramírez et al. 2013a). A total exposure of 2 × 900 s was obtained with the R300B grating. The fit to the Ly α line is shown in Fig. A15. The precise redshift is known from the Ly α emission line in a late-time spectrum of the host.
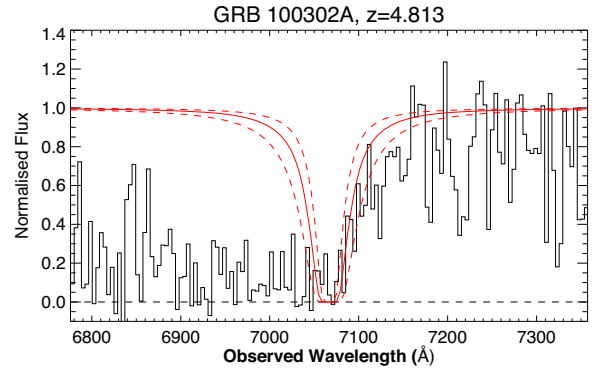
Figure A14. Fit of the red wing of Ly α for the GRB 100302A Gemini/GMOS spectrum.
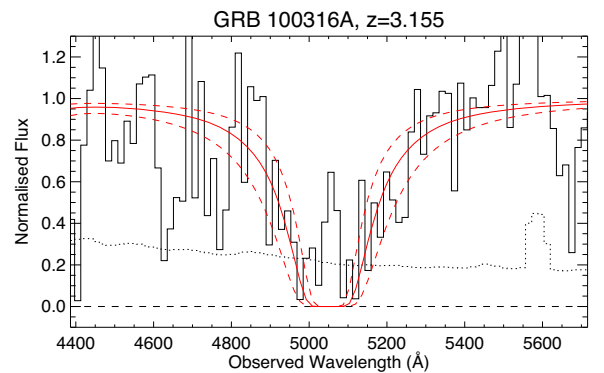
Figure A15. Fit of the red wing of Ly α for the GRB 100316A GTC/OSIRIS spectrum. Ly α line emission from the host galaxy is evident in the absorption trough, but does not affect the fit.
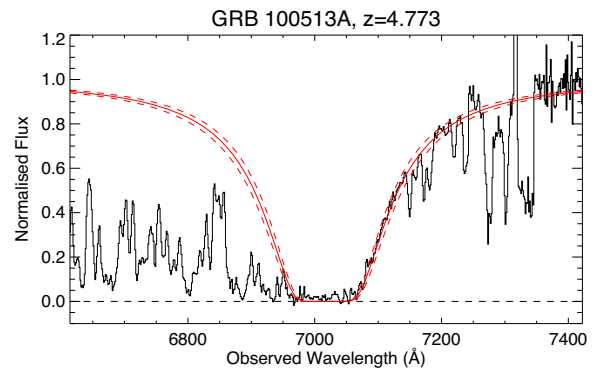
Figure A16. Fit of the red wing of Ly α for the GRB 100513A Gemini/GMOS-N spectrum. The large dips redwards of the Ly α line are residuals due to gaps between the detectors in the spectrograph.

A22 GRB 100513A

GRB 100513A was observed by Gemini/GMOS-N, starting 06:13 UT on 2010 May 13 (Cenko et al. 2010). A total exposure of 2 × 1200 s was obtained with the R400 grating set at 8000 Å central wavelength and reduced using the standard Gemini reduction tools within IRAF. The fit to the Ly α line is shown in Fig. A16.

Figure A17. Fit of the red wing of Ly α for the GRB 110731A Gemini/GMOS-N spectrum. The apparent feature at 4800 Å is due to the gap between the detectors in the spectrograph.

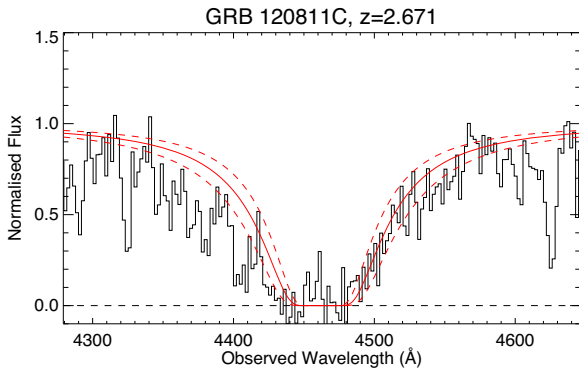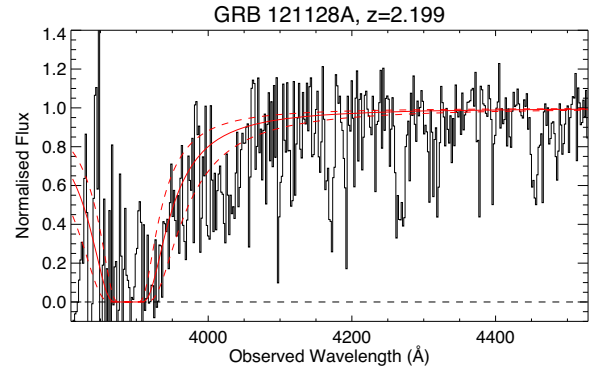**Figure A18.** Fit of the red wing of Ly α for the GRB 120811C GTC/OSIRIS spectrum.

A23 GRB 110731A

GRB 110731A was observed by Gemini/GMOS-N, starting 09:08 UT on 2011 August 1 (Tanvir et al. 2011). A total exposure of 4×900 s was obtained with the B600 grating set at 5250 Å central wavelength and reduced using the standard Gemini reduction tools within IRAF. The fit to the Ly α line is shown in Fig. A17.

A24 GRB 120811C

GRB 120811C was observed by the GTC/OSIRIS, starting 15:35 UT on 2012 August 11 (Thöne et al. 2012). A total exposure time of 2400 s was obtained, spanning a wavelength range 3640–7875 Å. The fit to the Ly α line is shown in Fig. A18. There is a possible hint of Ly α emission in the trough, but the S/N is not sufficient to be confident.

A25 GRB 121027A

GRB 121027A has been suggested as a member of the 'ultra-long' class of GRBs, whose exact nature remains uncertain, but since they also appear to be associated with massive stars in low-metallicity galaxies (Levan et al. 2014; Greiner et al. 2015a; Kann et al. 2018), we include it in our sample.

Figure A19. Fit of the red wing of Ly α for the GRB 121128A Gemini/GMOS-N spectrum.
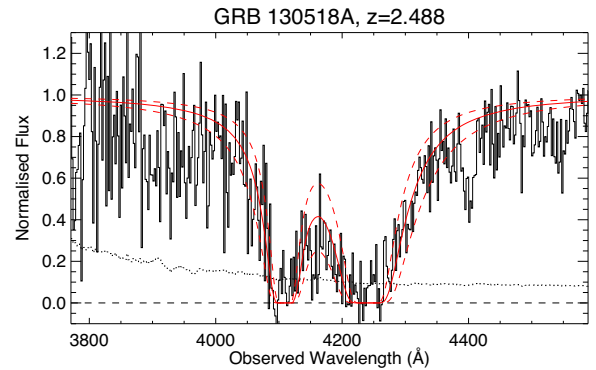
Figure A20. Fit of the red wing of Ly α for the GRB 130518A GTC/OSIRIS spectrum. A second, intervening DLA, at $z = 2.38$ is apparent.

A26 GRB 121128A

GRB 121128A was observed by Gemini/GMOS-N, starting 06:28 UT on 2012 November 28 (Tanvir, Levan & Matulonis 2012b). A total exposure of 4×400 s was obtained with the B600 grating set at 5250 Å central wavelength and reduced using the standard Gemini reduction tools within IRAF. The fit to the Ly α line is shown in Fig. A19.

A27 GRB 130518A

GRB 130518A was observed at high resolution with GTC/OSIRIS, starting 04:47 UT on 2013 May 20. A total exposure time of 840 s was obtained, spanning a wavelength range 3700–7800 Å and was originally reported in Sanchez-Ramirez et al. (2013b). The fit to the Ly α line is shown in Fig. A20.

A28 GRB 130610A

GRB 130610A was observed at high resolution with VLT/UVES, starting 03:25 UT on 2013 June 10 (Smette et al. 2013). A series of exposures were obtained totalling 6500 s. The fit to the Ly α line is shown in Fig. A21.

A29 GRB 131108A

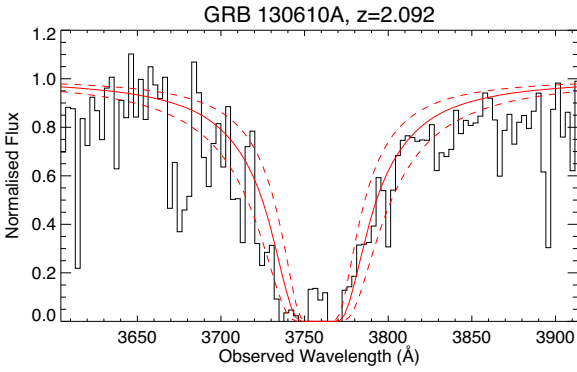GRB 131108A was observed with the GTC/OSIRIS, starting 20:42 UT on 2013 November 8 (de Ugarte Postigo et al. 2013). A total

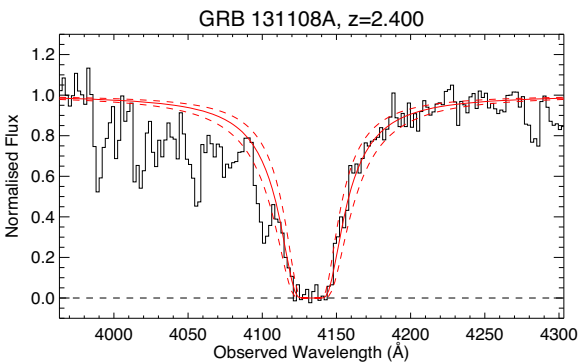**Figure A21.** Fit of the red wing of Ly α for the GRB 130610A VLT/UVES spectrum.

Figure A22. Fit of the red wing of Ly α for the GRB 131108A GTC/OSIRIS spectrum.

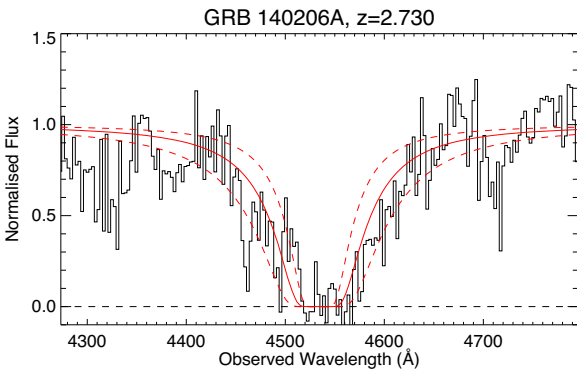**Figure A23.** Fit of the red wing of Ly α for the GRB 140206A NOT/ALFOSC spectrum.

exposure of 1800 s was obtained covering a spectral range 3700–7870 Å. The fit to the Ly α line is shown in Fig. A22.

A30 GRB 140206A

GRB 140206A was observed with the NOT/ALFOSC starting 19:56 UT on 2014 February 6 (Malesani et al. 2014; see also D'Elia et al. 2014 for TNG/DOLoRes spectroscopy). A total exposure of 3600 s was obtained covering a spectral range 3750–9000 Å. The fit to the Ly α line is shown in Fig. A23.
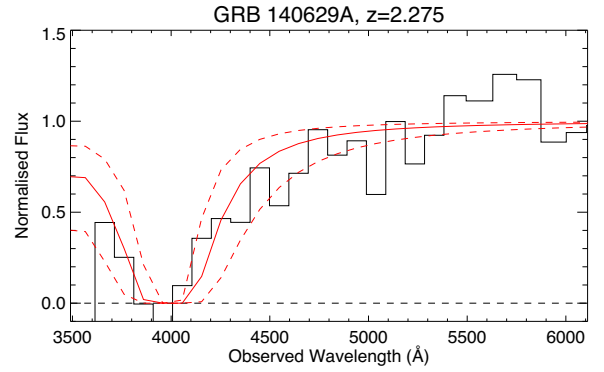
Figure A24. Fit of the red wing of Ly α for the GRB 140629A TNG/DOLoRes spectrum.

A31 GRB 140515A

GRB 140515A was a high redshift burst observed at several facilities. No metal lines were confidently detected so the redshift could only be estimated from the Ly α break itself. This limits the conclusions that can be drawn, since the damping wing must be decomposed into ISM and IGM contributions, which is less certain in the absence of a precise redshift. Nonetheless, the sharpness of the break clearly indicates a relatively low H I column density. Chornock et al. (2014) obtained a value of $\log(N_{\rm HI}/\rm cm^{-2}) = 18.62 \pm 0.08$ assuming an ionized IGM and $\log(N_{\rm HI}/\rm cm^{-2}) = 18.43$ in a joint fit including a neutral IGM component from an early Gemini-N/GMOS spectrum. Melandri et al. (2015) analysed later GTC and VLT spectroscopy and concluded $\log(N_{\rm HI}/\rm cm^{-2}) < 18.5$ whereas Selsing et al. (2018) estimate $\log(N_{\rm HI}/\rm cm^{-2}) = 19.0 \pm 0.5$. In this paper we therefore adopt a compromise value of $\log(N_{\rm HI}/\rm cm^{-2}) = 18.5 \pm 0.3$.

A32 GRB 140629A

GRB 140629A was observed with the TNG/DOLoRes, starting 02:07 UT on 2014 June 30 (D'Avanzo et al. 2014). A total exposure of 1200 s was obtained, covering a spectral range 3000–8000 Å. The fit to the Ly α line is shown in Fig. A24.

A33 GRB 140703A

GRB 140703A was observed with the GTC/OSIRIS, starting 03:16 UT on 2014 July 3. A total exposure of 450 s was obtained covering a spectral range 3700–10 000 Å and was originally reported in Castro-Tirado et al. (2014). The fit to the Ly α line is shown in Fig. A25.

A34 GRB 140808A

GRB 140808A was observed with the GTC/OSIRIS, starting 00:54 UT on 2014 August 8 (Gorosabel et al. 2014). A total exposure of 3600 s was obtained covering a spectral range 3700–7800 Å. The fit to the Ly α line is shown in Fig. A26.

A35 GRB 150413A

GRB 150413A was observed with the Asiago(CT)/AFOSC, starting 20:53 UT on 2015 April 13 (de Ugarte Postigo & Tomasella 2015). A total exposure of 1800 s was obtained covering a wavelength range 3400–8200 Å. The fit to the Ly α line is shown in Fig. A27.
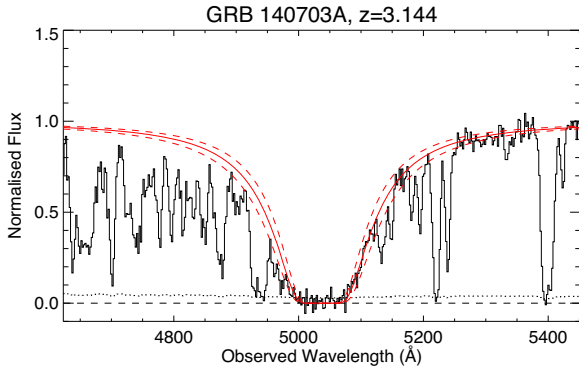
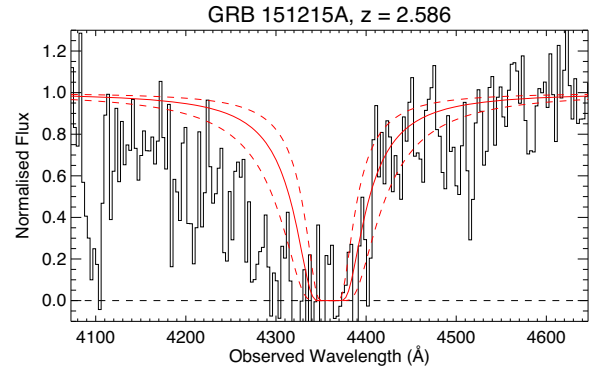**Figure A25.** Fit of the red wing of Ly α for the GRB 140703A GTC/OSIRIS spectrum.

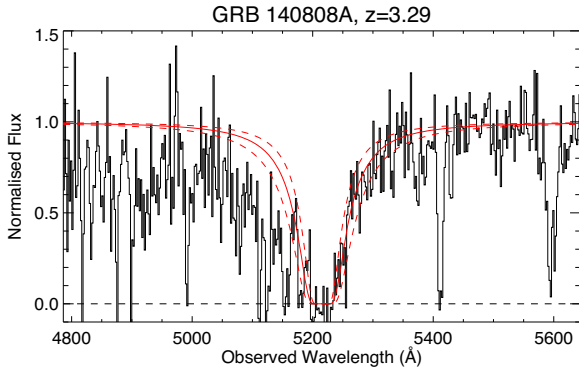**Figure A26.** Fit of the red wing of Ly α for the GRB 140808A GTC/OSIRIS spectrum.

Figure A27. Fit of the red wing of Ly α for the GRB 150413A CT/AFOSC spectrum.

Figure A28. Fit of the red wing of Ly α for the GRB 151215A NOT/ALFOSC spectrum.

Figure A29. Fit of the red wing of Ly α for the GRB 160227A NOT/ALFOSC spectrum.
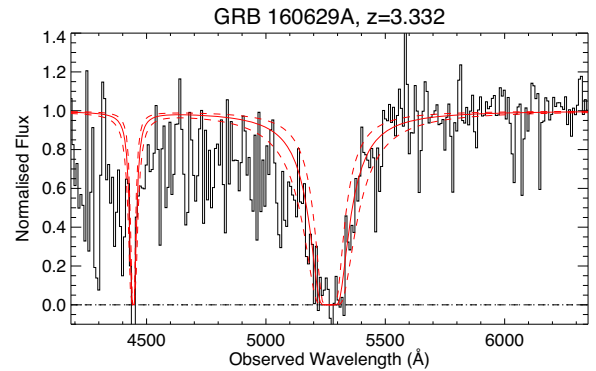
Figure A30. Fit of the red wing of Ly α for the GRB 160629A GTC/OSIRIS spectrum.

A36 GRB 151215A

GRB 151215A was observed with the NOT/ALFOSC, starting 04:13 UT on 2015 December 15 (Xu et al. 2015). A total exposure of 3 × 1200 s was obtained covering a spectral range 3200–9000 Å. The fit to the Ly α line is shown in Fig. A28.

A37 GRB 160227A

GRB 160227A was observed with the NOT/ALFOSC, starting at 20:19 UT on 2016 February 27 (Xu et al. 2016b). A total exposure

of 4800 s was obtained covering a wavelength range 3200–9000 Å. The fit to the Ly α line is shown in Fig. A29.

A38 GRB 160629A

GRB 160629A was observed with the GTC/OSIRIS, starting at 04:40 UT on 2016 June 30 (Castro-Tirado et al. 2016). A total exposure of 600 s was obtained covering a wavelength range 3700–7880 Å. The fit to the Ly α line is shown in Fig. A30.

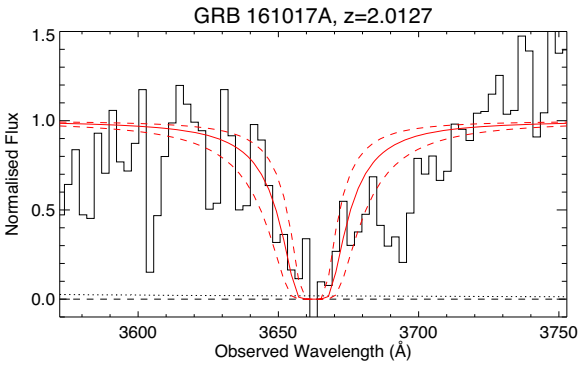**Figure A31.** Fit of the red wing of Ly α for the GRB 161017A TNG/DOLoRes spectrum.

Figure A33. Fit of the red wing of Ly α for the GRB 170531B GTC/OSIRIS spectrum.

Figure A32. Fit of the red wing of Ly α for the GRB 170405A GTC/OSIRIS spectrum.
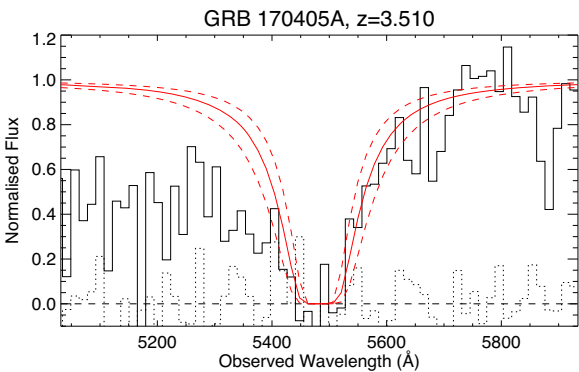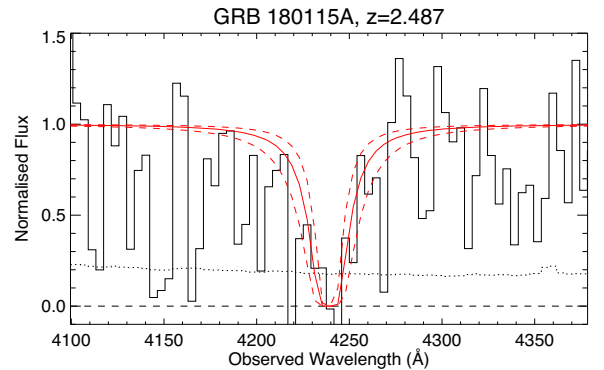

Figure A34. Fit of the red wing of Ly α for the GRB 180115A GTC/OSIRIS spectrum.

A39 GRB 161017A

GRB 161017A was observed with the TNG/DOLoRes, starting at 04:27 UT on 2016 October 18 (D'Avanzo et al. 2016). A total exposure of 1200 s was obtained covering a wavelength range 3500–8000 Å. The fit to the Ly α line is shown in Fig. A31.

For this GRB we also conducted a host search using the WHT/ACAM on 2017 April 7. In seeing of 1.1 arcsec we obtained a 45 min integration in the *g* band. No source was detected at the GRB position down to a 2σ limiting magnitude of *g* = 24.70, which is corrected for foreground Milky Way extinction (Schlafly & Finkbeiner 2011).

A40 GRB 170405A

GRB 170405A was observed with the GTC/OSIRIS, starting at 02:14 UT on 2017 April 6 (de Ugarte Postigo et al. 2017a). A total exposure of 3 × 900 s was obtained covering a wavelength range 3700–7800 Å. The fit to the Ly α line is shown in Fig. A32.
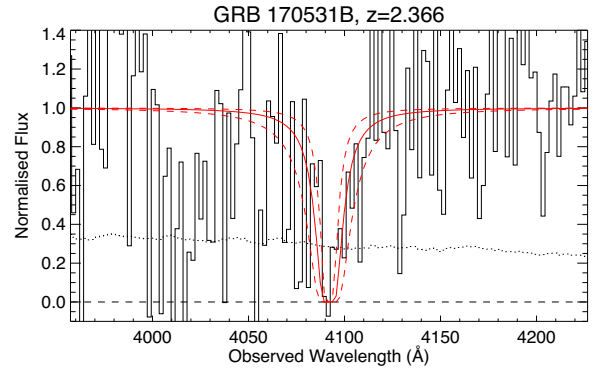
A41 GRB 170531B

GRB 170531B was observed with the GTC/OSIRIS, starting at 02:47 UT on 2017 June 1 (de Ugarte Postigo et al. 2017b). A total exposure of 3 × 900 s was obtained covering a wavelength range 3700–7880 Å. The fit to the Ly α line is shown in Fig. A33.

A42 GRB 180115A

GRB 180115A was observed with the GTC/OSIRIS, starting at 20:32 UT on 2018 June 15 (de Ugarte Postigo et al. 2018). A total exposure of 3 × 900 s was obtained covering a wavelength range 3700–7880 Å. The fit to the Ly α line is shown in Fig. A34. In this case, no metal lines were detected, so the redshift is based solely on Ly α.

A43 GRB 180329B

GRB 180329B was observed with the VLT/X-shooter, starting at 00:10 UT on 2018 March 30 (Izzo et al. 2018). A total exposure of 2 × 600 s was obtained covering a wavelength range 3000–21 000 Å. The fit to the Ly α line is shown in Fig. A35.

A44 GRB 180624A

GRB 180624A was observed with the LBT/MODS, starting at 10:15 UT on 2018 June 25 (Rossi et al. 2018). A total exposure of 2 × 600 s was obtained covering a wavelength range 3200–10 000 Å. The fit to the Ly α line is shown in Fig. A36.

A45 GRB 181020A

GRB 181020A was observed with the VLT/X-shooter, starting at 00:43 UT on 2018 October 21 (Fynbo et al. 2018). A total exposure of 4 × 600 s was obtained covering a wavelength range 3000–21 000 Å. The fit to the Ly α line is shown in Fig. A37.
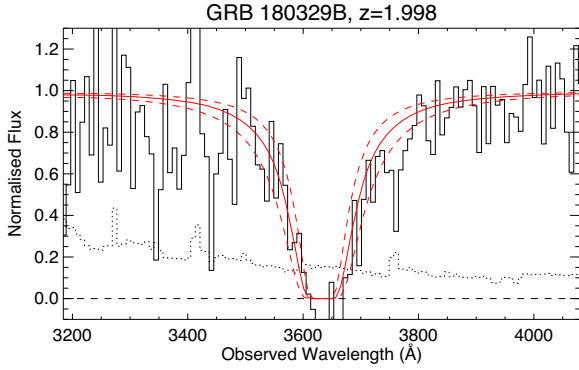
GRB 180329B, z=1.998

Figure A35. Fit of the red wing of Ly α for the GRB 180329B VLT/X-shooter spectrum.

GRB 180624A, z=2.855
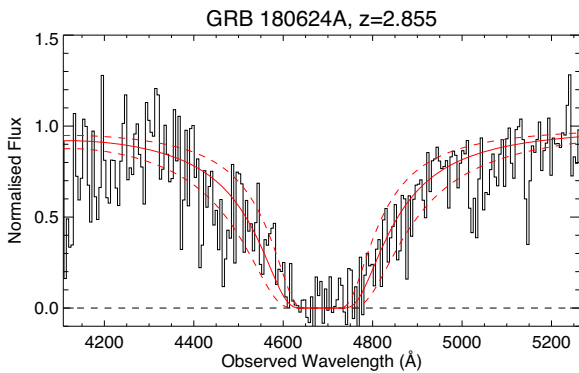
Figure A36. Fit of the red wing of Ly α for the GRB 180624A LBT/MODS spectrum.
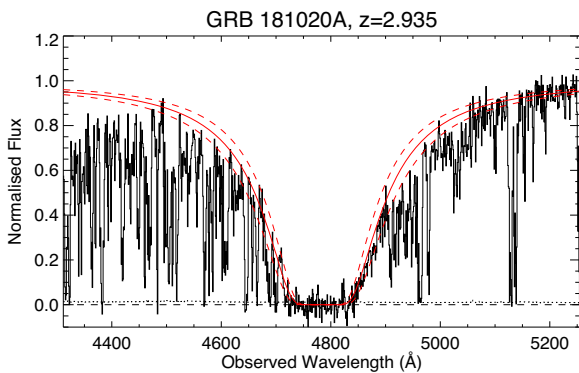
GRB 181020A, z=2.935

Figure A37. Fit of the red wing of Ly α for the GRB 181020A VLT/X-shooter spectrum.

[1]*Department of Physics & Astronomy and Leicester Institute of Space & Earth Observation, University of Leicester, University Road, Leicester LE1 7RH, UK*

[2]*Dark Cosmology Centre, Niels Bohr Institute, University of Copenhagen, Juliane Maries Vej 30, DK-2100 Copenhagen Ø, Denmark*

[3]*Instituto de Astrofísica de Andalucía (IAA-CSIC), Glorieta de la Astronomía s/n, E-18008 Granada, Spain*

[4]*Astronomical Institute Anton Pannekoek, University of Amsterdam, PO Box 94249, NL-1090 GE Amsterdam, the Netherlands*

[5]*Department of Physics, University of Warwick, Coventry CV4 7AL, UK*

[6]*Astrophysics Research Institute, Liverpool John Moores University, IC2, Liverpool Science Park, 146 Brownlow Hill, Liverpool L3 5RF, UK*

[7]*NASA's Goddard Space Flight Center, Greenbelt, MD 20771, USA*

[8]*Joint Space-Science Institute, University of Maryland, College Park, MD 20742, USA*

[9]*Harvard-Smithsonian Center for Astrophysics, 60 Garden Street, Cambridge, MA 02138, USA*

[10]*Astrophysical Institute, Department of Physics and Astronomy, Ohio University, Athens, OH 45701, USA*

[11]*INAF-Osservatorio Astronomico di Brera, Via Bianchi 46, I-23807 Merate, Italy*

[12]*College of Science and Mathematics, University of the Virgin Islands, #2 Brewers Bay Road, Charlotte Amalie, USVI 00802*

[13]*INAF - Osservatorio Astronomico di Roma, Via Frascati 33, 00040, I-00078, Monte Porzio Catone (RM), Italy*

[14]*ASI-Science Data Centre, Via del Politecnico, snc, I-00133 Rome, Italy*

[15]*INAF-IASF Milano, Via E. Bassini 15, I-20133 Milano, Italy*

[16]*APC, Astroparticule et Cosmologie, Université Paris Diderot, CNRS/IN2P3, CEA/Irfu, Observatoire de Paris, Sorbonne Paris Cité, 10, Rue Alice Domon et Léonie Duquet, F-75205 Paris Cedex 13, France*

[17]*Centre for Astrophysics and Cosmology, University of Nova Gorica, Vipavska 11c, 5270 Ajdovščina, Slovenia*

[18]*Centre for Astrophysics and Cosmology, Science Institute, University of Iceland, Dunhagi 5, 107 Reykjavík, Iceland*

[19]*Max-Planck-Institut für Extraterrestrische Physik, Giessenbachstrasse, D-85748 Garching, Germany*

[20]*Department of Physics, University of Bath, Claverton Down, Bath BA2 7AY, UK*

[21]*Department of Astronomy, University of California, 501 Campbell Hall, Berkeley, CA 94720-3411, USA*

[22]*Istituto di Astrofisica Spaziale E Fisica Cosmica di Bologna Area della Ricerca, via Piero Gobetti, 101, I-40129 Bologna, Italy*

[23]*Department of Particle Physics and Astrophysics, Weizmann Institute of Science, Rehovot 7610001, Israel*

[24]*Heidelberger Institut für Theoretische Studien, Schloss-Wolfsbrunnenweg 35, D-69118 Heidelberg, Germany*

[25]*GEPI, Observatoire de Paris, PSL Research University, CNRS, Univ. Paris Diderot, Sorbonne Paris Cité, Place Jules Janssen, F-92195 Meudon, France*

[26]*Department of Astrophysics, Radboud University Nijmegen, P.O. Box 9010, NL-6500 GL Nijmegen, The Netherlands*

[27]*CAS Key Laboratory of Space Astronomy and Technology, National Astronomical Observatories, Chinese Academy of Sciences, Beijing 100012, China*

This paper has been typeset from a TEX/LATEX file prepared by the author.